JGR Solid Earth

RESEARCH ARTICLE
10.1029/2024JB029862

Characterizing Sub-Seafloor Seismic Structure of the Alaska Peninsula Along the Alaska-Aleutian Subduction Zone

Mengjie Zheng[1,2], Anne F. Sheehan[1,2], Chuanming Liu[3], Mengyu Wu[4,5], and Michael H. Ritzwoller[4]

[1]Cooperative Institute for Research in Environmental Sciences, University of Colorado Boulder, Boulder, CO, USA, [2]Department of Geological Sciences, University of Colorado Boulder, Boulder, CO, USA, [3]Institute for Geophysics and Department of Earth and Planetary Sciences, Jackson School of Geosciences, The University of Texas at Austin, Austin, TX, USA, [4]Department of Physics, University of Colorado Boulder, Boulder, CO, USA, [5]Now at Viridien, Houston, TX, USA

Key Points:

- Sub-seafloor Vs model offshore the Alaska Peninsula is constructed using a joint inversion of seafloor compliance and Ps delays
- Seismic properties of the seafloor sediments correlate with lithological composition, with the deep-sea sediments showing reduced Vs
- The upper oceanic crust of the Semidi exhibits lower Vs than the Shumagin, possibly related to different seafloor spreading rates

Supporting Information:

Supporting Information may be found in the online version of this article.

Correspondence to:

M. Zheng and A. F. Sheehan,
Mengjie.Zheng@colorado.edu;
Anne.Sheehan@colorado.edu

Citation:

Zheng, M., Sheehan, A. F., Liu, C., Wu, M., & Ritzwoller, M. H. (2024). Characterizing sub-seafloor seismic structure of the Alaska Peninsula along the Alaska-Aleutian subduction zone. *Journal of Geophysical Research: Solid Earth*, *129*, e2024JB029862. https://doi.org/10.1029/2024JB029862

Received 9 JUL 2024
Accepted 12 NOV 2024

Author Contributions:

Conceptualization: Mengjie Zheng, Anne F. Sheehan, Michael H. Ritzwoller
Data curation: Mengjie Zheng
Formal analysis: Mengjie Zheng
Funding acquisition: Anne F. Sheehan, Michael H. Ritzwoller
Investigation: Mengjie Zheng, Anne F. Sheehan
Methodology: Mengjie Zheng, Anne F. Sheehan, Chuanming Liu, Mengyu Wu, Michael H. Ritzwoller
Project administration: Anne F. Sheehan, Michael H. Ritzwoller
Resources: Anne F. Sheehan
Software: Mengjie Zheng
Supervision: Anne F. Sheehan, Michael H. Ritzwoller
Validation: Mengjie Zheng
Visualization: Mengjie Zheng, Anne F. Sheehan

Abstract A shallow sub-seafloor seismic model that includes well-determined seismic velocities and clarifies sediment-crust discontinuities is needed to characterize the physical properties of marine sediments and the oceanic crust and to serve as a reference for deeper seismic modeling endeavors. This study estimates the seismic structure of marine sediments and the shallow oceanic crust of the Alaska-Aleutian subduction zone at the Alaska Peninsula, using data from the Alaska Amphibious Community Seismic Experiment (AACSE). We measure seafloor compliance and Ps converted wave delays from AACSE ocean-bottom seismometers (OBS) and seafloor pressure data and interpret these measurements using a joint Bayesian Monte Carlo inversion to produce a sub-seafloor S-wave velocity model beneath each available OBS station. The sediment thickness across the array varies considerably, ranging from about 50 m to 2.80 km, with the thickest sediment located in the continental slope. Lithological composition plays an important role in shaping the seismic properties of seafloor sediment. Deep-sea deposits on the incoming plate, which contain biogenic materials, tend to have reduced S-wave velocities, contrasting with the clay-rich sediments in the shallow continental shelf and continental slope. A difference in S-wave velocities is observed for upper oceanic crust formed at fast-rate (Shumagin) and intermediate-rate (Semidi) spreading centers. The reduced S-wave velocities in the Semidi crust may be caused by increased faulting and possible lithological variations, related to a previous period of intermediate-rate spreading.

Plain Language Summary Sediment input has been regarded as a "lubricant" that smooths the subduction interface, allowing earthquakes to rupture over large horizontal distances and resulting in large earthquakes. Variations in sediment properties have been correlated with heterogeneity in the intensity and frequency of earthquakes along the Alaska-Aleutian subduction zone. Here, we produce a shear-wave velocity (Vs) model of seafloor sediment and the shallow oceanic crust along the Alaska Peninsula using ocean-bottom seismic and seafloor pressure data from the Alaska Amphibious Community Seismic Experiment. Lithological composition significantly influences the seismic properties of seafloor sediment, and the deep-sea seafloor sediments that include biogenic materials are characterized by reduced Vs, differing from the shallow-water clay-rich sediments. In addition, we observe a difference in the shear-wave velocity of the shallow oceanic crust between the Shumagin and Semidi segments of the Alaskan margin, which might be evidence of varying seafloor spreading rates during previous plate reorganizations.

1. Introduction

A well-determined sub-seafloor structure, encompassing both seafloor sediment and shallow crystalline crust, is essential to understand regional geological and tectonic processes and provides critical insights into various geohazards and their triggers. In particular, characterizing seafloor sediment is pivotal for correlating lithological variations (Alibés et al., 1999; Madrussani et al., 2018), evaluating ground-motion amplification effects (Gomberg, 2018; Kaneko et al., 2019), modeling tsunamis (Ma & Nie, 2019), and understanding the seismogenic properties of megathrusts in subduction zones (Bilek & Lay, 2018; Brizzi et al., 2020). Additionally, illuminating sub-seafloor structures aids in identifying areas of resource interest such as mineral deposits (Olakunle et al., 2021; Rona, 2003) and gas hydrates (Francisca et al., 2005; Roberts et al., 2006) and serves offshore activities such as planning, designing, and operating marine infrastructure (Vanneste et al., 2014). Accurate

Writing – original draft: Mengjie Zheng
Writing – review & editing: Mengjie Zheng, Anne F. Sheehan, Chuanming Liu, Mengyu Wu, Michael H. Ritzwoller

knowledge of seafloor sediment thickness and seismic velocities also is critical for modeling the sediment layer reverberations that dominate the ocean-bottom seismometer (OBS) receiver function analysis (Audet, 2016; Kim et al., 2021; Zhang & Olugboji, 2021).

Much of our current knowledge on sub-seafloor structures is based on drilling observations and marine active source seismic data. While these methods offer detailed information, they are costly and thus usually result in limited spatial sampling. In the Alaska Peninsula region, active-source seismic experiments, such as the Alaska Langseth Experiment to Understand the megaThrust (ALEUT), provide critical constraints on the shallow sub-seafloor seismic structure. These observations have revealed spatial variations in physical properties of both incoming (Shillington et al., 2015) and subducted sediments (Bécel et al., 2017; Li et al., 2018; Shillington et al., 2015), leading to the hypothesis that sediment inputs contribute to along-strike variations in seismicity within the Aleutian-Alaska subduction zone. However, active-source seismic imaging mainly yields a P-wave velocity model and often lacks estimates of S-wave velocities, which limits information that may constrain porosity, consolidation state, elevated pore fluid pressures, and crack properties (Zhu et al., 2020). Moreover, the trade-off between seismic velocities and discontinuities in marine seismic imaging remains a challenge (Bell et al., 2015; Doran & Laske, 2019; Ruan et al., 2014). In addition, a well-defined sub-seafloor model which includes sediment thickness and seismic velocities is crucial not only to characterize the physical properties of seafloor sediments but also to correct and account for its influence in seismic data used to investigate deeper structures (Saikia et al., 2020).

In this paper, we use ocean-bottom seismometer (OBS) data from the Alaska Amphibious Community Seismic Experiment (AACSE, Barcheck et al. (2020), Figure 1a) to determine the in-situ S-wave velocities and sediment thickness beneath each available AACSE OBS station. We do this through a Monte Carlo joint inversion of seafloor compliance and Ps converted wave delays. The estimated sub-seafloor S-wave velocity model offers valuable constraints on the properties of seafloor sediments and the shallow oceanic crust and can also serve as a reference for future studies such as deeper seismic imaging and tsunami modeling.

2. Geological Background

The Alaska-Aleutian subduction zone (AASZ) is a convergent plate boundary where the Pacific Plate is subducting beneath the North American Plate. The Alaska Peninsula section of the AASZ, located in the northeast, is characterized by its high level of seismic activity, including several great earthquakes ($M > 8.0$) over the past century (Brocher et al., 2014; Ryan et al., 2012), such as the 1964 M9.2, 1938 M8.2, and 1946 M8.6 earthquakes (Figure 1b). The observation of spatial and temporal patterns of these large earthquakes has led to the idea that the Alaska Peninsula megathrust is segmented (Nishenko & Jacob, 1990) with different segments, including Kodiak, Semidi, and Shumagin (Figure 1), having different earthquake cycles (Ramos et al., 2022).

Along the strike of the Alaska Peninsula, the large-scale characteristics of plate structure and kinematics such as the convergence rate (63 mm/yr, Sella et al. (2002)), direction, and plate age (~55 Ma, Müller et al. (2008)), are relatively constant, as is the thermal state of the subducted slab (Clarke et al., 2024). Despite this uniformity, there are other along-strike variations, including in present-day plate coupling (Drooff & Freymueller, 2021), the frequency and intensity of seismicity (Shillington et al., 2015; Wei et al., 2021), arc magmatism (Kelemen et al., 2004; Lopez et al., 2023), as well as seismic anisotropy (Liu et al., 2022). Geodetic studies (Drooff & Freymueller, 2021; Li et al., 2016; Li & Freymueller, 2018) have inferred significant transitions in coupling along strike, from strong locking in the Kodiak segment, through intermediate locking in the Semidi segment, to weak locking (creeping) in the Shumagin segment. The Semidi segment historically hosted several great earthquakes but has relatively sparse background seismicity (Shillington et al., 2015), while the Shumagin segment, where a double seismic zone is observed (Abers, 1992; Shillington et al., 2015), features a high frequency of seismicity with $M < 7.0$.

For the subduction zone, many factors have been hypothesized to contribute to megathrust spatial heterogeneity and slip variability, including pre-existing seafloor fabric (Shillington et al., 2015), trench-ridge angle (Fujie et al., 2018), slab curvature (Naliboff et al., 2013), and the presence of fluids and sediments, among others (Bilek and Lay (2018) and references therein). These factors are intricately interconnected, influencing the seismogenic properties of the subduction zone in complex ways. For example, pre-existing seafloor fabric affects seismicity through incoming plate hydration (Shillington et al., 2015), the hydration accompanied with plate bending constitutes a major source of water for the subduction zone (Cai et al., 2018; Li et al., 2024), and fluids within the

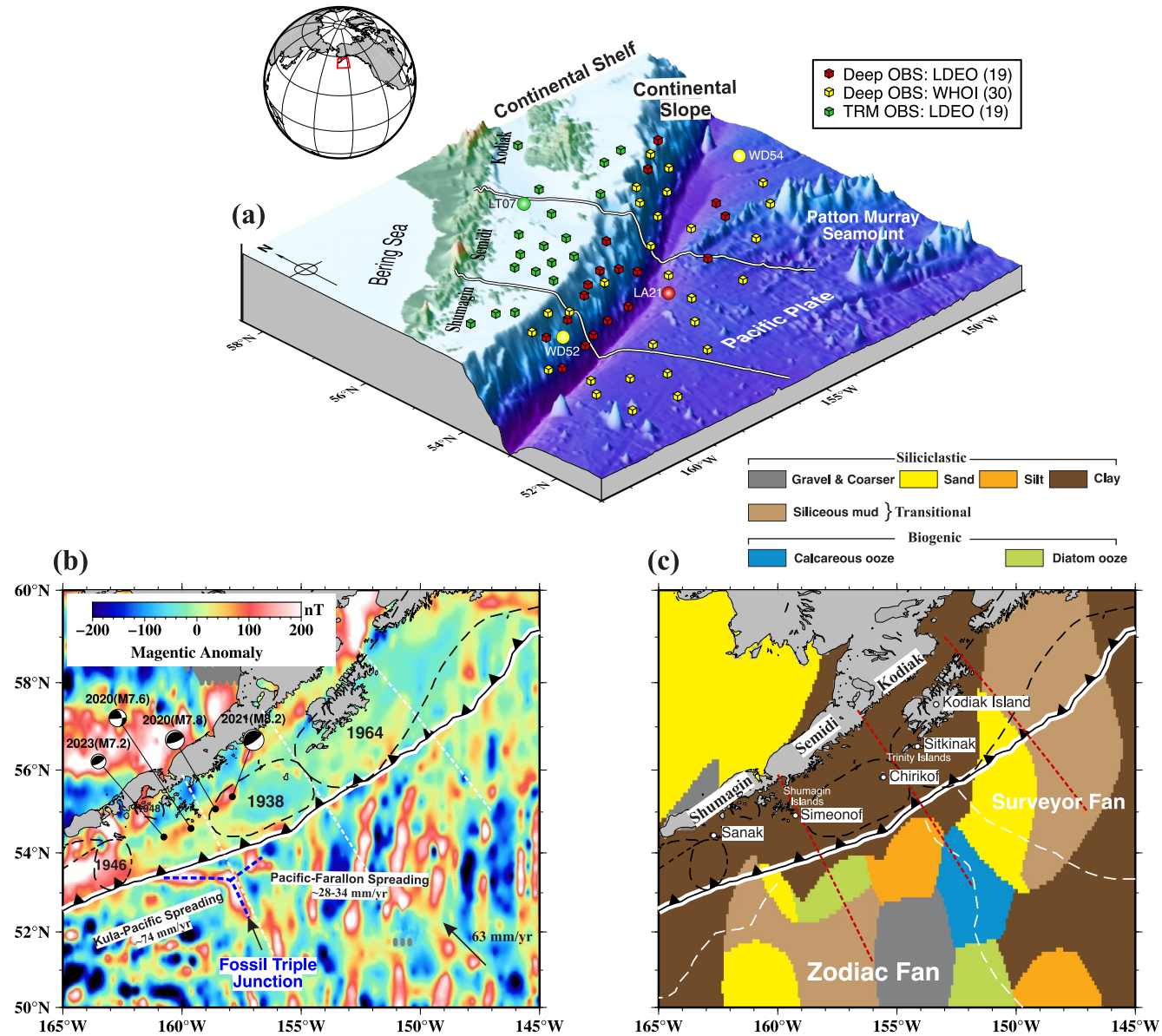

Figure 1. (a) Oblique view of the Alaska-Aleutian subduction zone along the Alaska Peninsula, showing the 68 ocean-bottom seismometers (OBS) used in this study. The white lines are the approximate boundaries between the Shumagin, Semidi, and Kodiak segments (Davies et al., 1981). Red cubes: Deep OBS, Lamont Doherty Earth Observatory; Green cubes: Trawl Resistant Mounted (TRM) OBS, Lamont Doherty Earth Observatory; Yellow cubes: Deep OBS, Woods Hole Oceanographic Institution. The number of stations is shown in the legend. The red rectangle in the upper left inset map marks the study region. (b) Magnetic anomaly map along the Alaska Peninsula. The blue dashed lines mark the T-shaped Anomaly (53 Ma), collated with the fossil triple junction left by the plate reorganizations. Adjacent to this anomaly, the Pacific–Farallon spreading to the east and Kula-Pacific spreading to the west, occurred at intermediate (half-rates of ∼28–34 mm/yr) and fast (half-rates of ∼74 mm/yr) spreading rates, respectively. White dashed lines are the approximate boundaries between the Shumagin, Semidi, and Kodiak segments, black dashed contours mark the rupture zones of previous great megathrust earthquakes (Tape, 2022). The beachballs are focal mechanisms of recent large Aleutian earthquakes (2020–2023). (c) Seafloor lithology map of the Alaska Peninsula (Dutkiewicz et al., 2015). The white dashed lines mark the approximate range of the Zodiac Fan and Surveyor Fan, red dashed lines are the approximate boundaries between the Shumagin, Semidi, and Kodiak segments.

overriding plate depend on how much water is input into the trench. For the Alaska Peninsula, key contributors that have been highlighted include the pre-existing seafloor fabric of the incoming plate (Guo et al., 2023; Li & Freymueller, 2018; Liu et al., 2024; Liu & Ritzwoller, 2024; Shillington et al., 2015), fluids within the overriding plate (Wang et al., 2024), and the input sediments. The findings obtained from active-source seismic experiments such as ALEUT suggest that the subducted sediment in the Semidi segment is thicker and more weakly disrupted, which may suppress the shallow megathrust slip due to the high-fluid pressure but favors the regular occurrence of

great earthquakes at the deeper megathrust (Li et al., 2018). Conversely, the Shumagin segment, with its thinner and heterogeneous sediment layer (Bécel et al., 2017; Shillington et al., 2015), may be linked to higher levels of seismic activity, evidence of creeping, and less regular great earthquakes (Li et al., 2018).

Additionally, the incoming sediment south of the trench, as a proxy for estimating the composition and properties of sediments subducted along the plate interface, is also characterized by along-strike variations in thickness (Ryan et al., 2012), composition (Kelemen et al., 2004), and lithology (Figure 1c, Dutkiewicz et al. (2015)). A trend marked by a decrease in sediment thickness (Ryan et al., 2012) and increased structural disruption due to outer-rise normal faulting is observed from the Semidi in the east to the Shumagin in the west (Shillington et al., 2015).

3. Data and Methods

The AACSE experiment, designed to sample the Alaska-Aleutian megathrust offshore of the Alaska Peninsula, offers a unique opportunity to illuminate the marine structures that span the incoming Pacific plate, the continental slope, and the shallow continental shelf in this region. A total of 75 broadband OBS stations were deployed from May 2018 to September 2019 in AACSE, and 68 stations were recovered with valid seismic and pressure data, which are used in this study. These 68 OBS stations (Figure 1a) are deployed at water depths ranging from 83 to 5,113 m. Each OBS is equipped either an Absolute Pressure Gauge (APG) or a Differential Pressure Gauge (DPG). Refer to Barcheck et al. (2020) for more information about instrument deployment details and data availability and quality.

3.1. Seafloor Compliance

Seafloor compliance is a measure of the seafloor's ability to deform elastically in response to pressure loads from infragravity waves (Crawford et al., 1991). Normalized seafloor compliance $\eta(\omega)$, is the transfer function between vertical displacement and seafloor pressure scaled by the wavenumber $k(\omega)$ of the forcing waves:

$$\eta(\omega) = k(\omega)\frac{S_d(\omega)}{S_p(\omega)} \tag{1}$$

where $S_d(\omega)$ and $S_p(\omega)$ are the displacement and pressure spectrum, respectively, and ω is the angular frequency (Crawford et al., 1991, 1998). In an isotropic uniform half-space, the seafloor compliance can be related to Lamé parameters λ and μ as follows (Crawford, 2004):

$$\eta(\omega) = k\frac{u}{\tau_{zz}} = \frac{\lambda+2\mu}{2\mu(\lambda+\mu)} = \frac{V_p^2}{2\rho V_s^2\left(V_p^2-V_s^2\right)} \tag{2}$$

where u and τ_{zz} are the displacement and stress component in the vertical direction at the seafloor, respectively. The seafloor compliance essentially is an in-situ point measurement, and the vertical motion is much more sensitive to μ (shear modulus) than to λ (Crawford et al., 1991). It has, therefore, been widely used to estimate in-situ S-wave velocities (Ball et al., 2014; Doran & Laske, 2019; Zha & Webb, 2016). The partial derivative of compliance with respect to the S-wave velocity is negative (Equation 3), suggesting that an increase in the S-wave velocity results in a decrease in compliance.

$$\frac{\partial\eta}{\partial V_s} = -\frac{V_p^2\left(V_p^2-2V_s^2\right)}{\rho V_s^3\left(V_p^2-V_s^2\right)^2} \tag{3}$$

3.1.1. Measuring Seafloor Compliance

The continuous vertical component seismic data and seafloor pressure data recorded by the OBS stations are segmented into daily intervals, resampled to 5 Hz, and instrument response is deconvolved, yielding seismic waveforms in displacement. Day-long recordings from both the vertical (Z) and pressure (P) components are used to calculate seafloor compliance. If two horizontal seismic components are available, a tilt correction (Crawford & Webb, 2000) is applied to the Z-component records. To ensure the reliability of the compliance measurements,

we first adopt a two-step automated quality-control (QC) procedure (Janiszewski et al., 2019), which is designed to identify and discard the daily recordings that may be contaminated by transient signals. The daily Power Spectral Density functions (PSDs) are estimated through Welch's method (Welch, 1967), and the daily Z- and P-component noise data are windowed into 2-hr segments with a 30% overlap. In the first-step QC, the calculated PSDs in the frequency range from 0.004 to 2 Hz are smoothed via a boxcar function, and segments deviating by more than 1.5 times the standard deviation from the daily average are discarded. Moreover, a 95% confidence level *F*-test, which compares the standard deviation of the PSDs with and without the discarded segments, is employed for additional QC validation. Subsequently, the retained PSDs are averaged to produce daily averaged PSDs. To identify the daily samples that are dominated by transient signals, a second-step QC is introduced (black filled box in Figure 2a). In this step, a comparison is made between the daily averaged PSDs and the PSD averaged over the whole deployment, using a similar standard deviation analysis coupled with a 95% confidence level *F*-test.

To further enhance the reliability of the measured compliance, we employ an enhanced QC based on the pressure-vertical coherence, a strategy widely acknowledged and utilized in compliance QC (Crawford et al., 1991; Doran & Laske, 2019; Zha & Webb, 2016). This also aids in determining the reliable frequency range for the infragravity wave response. The upper cut-off frequency f_c (right black dashed line in Figure 2d) can be calculated based on water depth following Equation 4 (Crawford et al., 1991):

$$f_c = \left[\frac{g}{2\pi Hn}\right]^{1/2}, 0.5 < n < 2 \tag{4}$$

where H is the water depth and g is gravitational acceleration. Starting with a presumed lower cut-off frequency f_0 (0.004 Hz), we apply a criterion wherein at least 30% of the measurements within the f_0 to f_c frequency range must exhibit a coherence greater than 0.8. For each station, we require at least 15 daily measurements retained in this criterion. The mean and standard deviation of these retained compliance data are subsequently calculated to represent the compliance measurement and quantify its uncertainty (Figure 2e). Additionally, the averaged coherence across these measurements is utilized to determine the tuned lower cut-off frequency, f_{tuned}, corresponding to the coherence threshold of 0.8 (Figure 2d). The compliance measurements within the f_{tuned} to f_c will be used for the S-wave velocity inversion.

We observe in particular that the retained daily compliances mainly occur from October of the first year (2018) to May of the following year (2019). Further analysis (Figure S4 in Supporting Information S1) confirms that this occurs broadly across these stations and reveals a "two-peak" pattern (in October and February) during this period. Moreover, this pattern is consistent across stations located on the shallow shelf, continental slope, and incoming plate, suggesting that it is not influenced by water depth or temporal variations in sub-seafloor properties. Instead, it may be related to broader environmental factors such as the transition between seasonal climatic conditions. The increased storm frequency and intensity (Stabeno et al., 2004) in the Alaska Peninsula during winter and spring may elevate the dynamic pressure at the seafloor, which facilitate the measurements of seafloor compliance (Wang et al., 2010).

3.1.2. DPG Gain Calibration

Through the two-step QC process and an enhanced coherence-based QC, we successfully measure seafloor compliance at 45 of the 68 AACSE OBS stations. Of the 45 stations with valid compliance measurements, 26 OBS stations are equipped with Differential Pressure Gauges (DPGs). The accuracy of compliance measurements using DPG may be compromised due to the ambiguity inherent in the DPG response function, which hampers our capacity to recover amplitude and phase information from seafloor pressure signals with high fidelity (Doran et al., 2019). To mitigate this issue and ensure that the calculated transfer functions between pressure and displacement can be converted to true compliance responses, we conduct an in-situ DPG gain calibration using teleseismic Rayleigh waves (Doran, 2019; Zha & Webb, 2016). Further details can be found in Supporting Information S1. The gain factors we estimate typically vary from 0.962 to 3.29, but with anomalously low values of ∼0.2 at station WS71, WS74, and WS75 (Table S1 in Supporting Information S1), suggesting a possible leaky valve in their DPGs (Zha & Webb, 2016). We then divide the initially measured compliance by the obtained gain factors to correct the amplitude, and Figure S3 in Supporting Information S1 shows the example at stations WD51 and WS71.

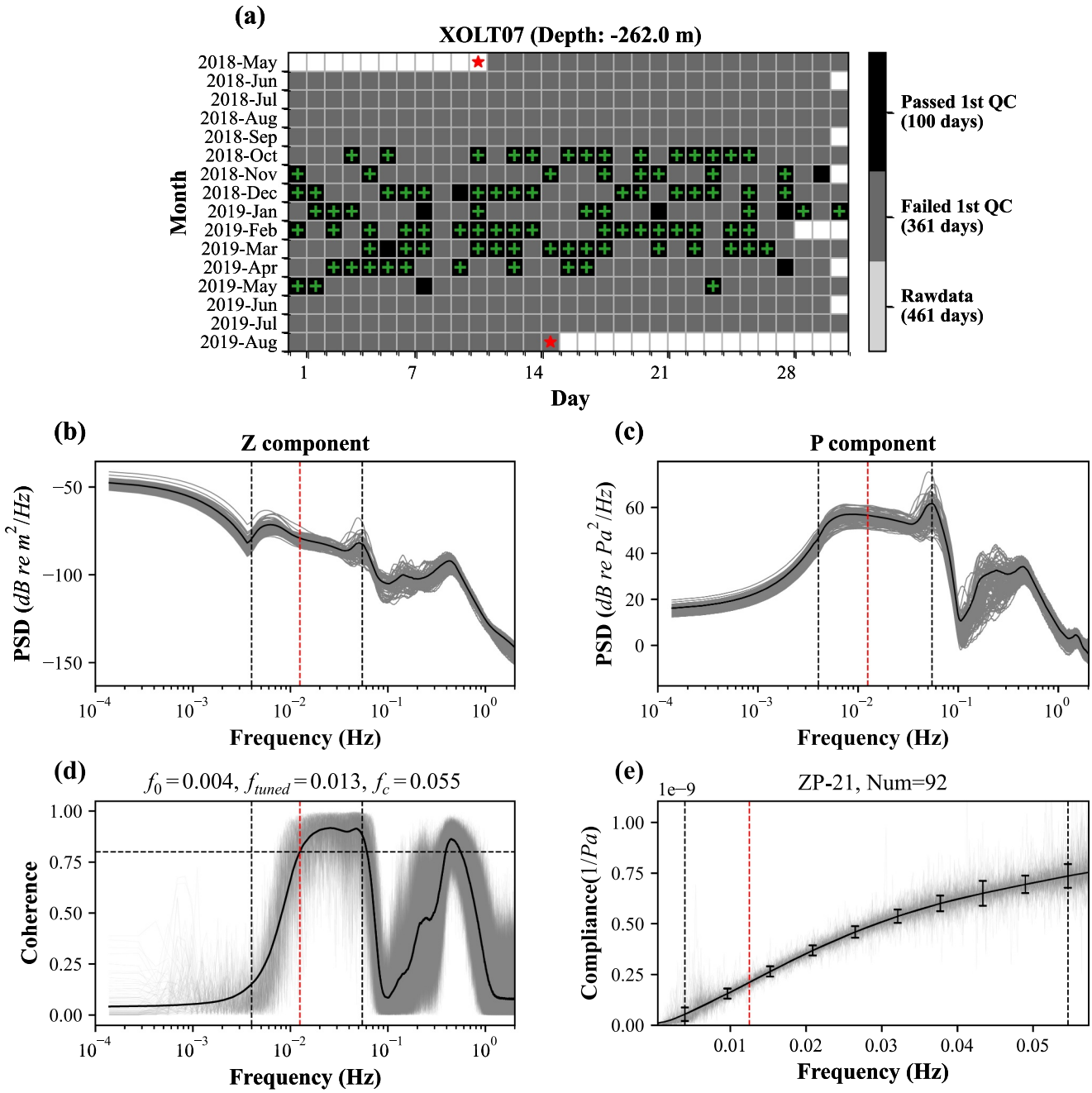

Figure 2. Example of measuring seafloor compliance at station LT07 (depth = −262.0 m), marked with green ball in Figure 1a (156.1199W, 56.6712N). (a) Quality Control (QC) statistics for compliance measurements. Red stars mark the start and end date of data availability for station LT07. Boxes with different fill colors illustrate the days retained after the two-step automated quality-control (QC) procedure. The green crosses indicate days that measurements are retained following QC based on P-Z coherence. (b) Daily Power Spectral Density (PSD) functions for the vertical component seismogram (gray lines). The black line denotes the averaged PSDs across the entire deployment. (c) Similar to (b) but for the pressure component. (d) The coherence functions between Z- and P-components of the retained compliance measurements (gray lines) and the averaged coherence function (black line). The horizontal dashed line in (d) indicates the coherence threshold of 0.8. (e) The retained compliance measurements (gray lines, 92 in total), and the averaged compliance function and its uncertainties (error bars). The ZP-21 (nomenclature from OBStools) compliance function, is calculated using the vertical seismogram that have been corrected for tilt and pressure. In (b)–(e), the red vertical dashed line denotes the tuned lower cut-off frequency, and the black vertical dashed lines on the left and right denote the frequency of 0.004 Hz and the upper cut-off frequency.

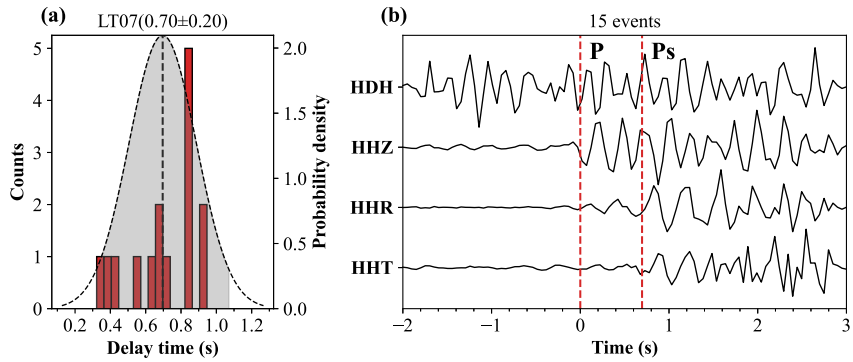

Figure 3. Ps delay measurements at station LT07. (a) The histogram of the measured Ps delay times, with a dual *y*-axis presentation of the associated Gaussian normal distribution curve. The shaded gray areas denote the range within two standard deviations. (b) The stacked waveforms from 15 different local earthquakes, with two vertical red dashed lines showing the measuring arrivals for P and Ps phases. HDH, HHZ, HHR, and HHT are pressure, vertical, radial, and transverse components, respectively.

3.2. Ps Converted Wave Delays

The sharp contrast in seismic properties between seafloor sediment and the underlying oceanic crust results in the conversion of upward propagating P-waves to S-waves, leading to a Ps converted phase on the horizontal component seismograms that arrives slightly later than the first arriving direct P on the vertical component seismogram. This delay is closely related to seafloor sediment properties, particularly to Vp/Vs ratio and thickness, which has been successfully used in seafloor sediment characterization (Agius et al., 2018; Chichester et al., 2020; Harmon et al., 2007). Moreover, simultaneously interpreting the Ps delay and compliance measurements has been demonstrated to be an effective strategy to mitigate ambiguities between S-wave velocity and the thickness of sediments (Doran & Laske, 2019). The theoretical Ps delay time is formulated as follows:

$$\mathrm{dt} = \mathrm{h}\left(\frac{\cos\theta_s}{V_s} - \frac{\cos\theta_p}{V_p}\right) \tag{5}$$

where h is sediment thickness, V_s and V_p are averaged S-wave and P-wave velocities, and θ_s and θ_p are their associated incident angles at the seafloor. Here we assume a nearly vertical incidence (i.e., $\cos\theta_s \approx \cos\theta_p \approx 1$) considering the high impedance contrast between seafloor sediment and oceanic crust.

Earthquakes with epicentral distances within 10° and with magnitudes $3.5 \le M \le 6.5$ during the time of observation are collected to measure the Ps delay time at each station, and the original waveforms are rotated to a ZRT system using the station orientations (Table S2 in Supporting Information S1) determined by Lynner (2021). Using a bandpass filter of 2.0–10.0 Hz, we manually pick the P-wave arrival time on the vertical and pressure components, as well as the Ps converted wave arrival time on the radial and transverse components. Only events with signal-to-noise ratio exceeding 10 and with clear P and Ps phases on vertical and horizontal components are included. For each event, the Ps delay time is calculated by averaging the arrival time differences between both vertical-radial and vertical-transverse component pairs. We first calculate the mean (μ) and standard deviation (σ) of the obtained measurements at each station, and measurements within twice the standard deviation ($\mu \pm 2\sigma$) are retained to enhance their reliability. Subsequently, the mean and standard deviation of the retained measurements are recalculated at the station, to represent the Ps delay time measurement and its uncertainty. Additionally, only stations with at least 10 Ps delay time measurements are considered. Figure 3 shows an example of Ps delay time measurements at station LT07.

3.3. Monte Carlo Joint Inversion of Seafloor Compliance and Ps Delays

We implement a Markov Chain Monte Carlo (MCMC) algorithm through PyMC (John et al., 2016) to estimate S-wave velocities beneath each available AACSE OBS station using seafloor compliance and Ps delay measurements. This approach helps circumvent the issue of getting trapped in local minima given the non-convex nature

of the 1-D depth inversion of the compliance function (Zha & Webb, 2016) and offers meaningful uncertainty estimates of the resolved structure. Synthetic compliance functions are computed using the 1-D forward modeling routine of Crawford et al. (1991) that is optimized by Mosher et al. (2021), and the Ps delay time is calculated by Equation 5.

3.3.1. The Joint Likelihood Function

The likelihood function $L(m)$ is derived from the misfit function $S(m)$ based on the assumption of Gaussian errors.

$$L(m) = exp\left(-\frac{1}{2}S(m)\right) \tag{6}$$

The joint misfit function $S_{joint}(m)$ of seafloor compliance and Ps delays is defined by the Chi-Square statistic:

$$S_{joint}(m) = S_{comply} + \frac{1}{\kappa}S_{Ps} = \sum_{i=1}^{N}\frac{\left(g_i(m) - D_i^{obs}\right)^2}{\sigma_i^2} + \frac{1}{\kappa}\sum\frac{\left(p(m) - S^{obs}\right)^2}{\delta^2} \tag{7}$$

Here $g_i(m)$ is the compliance function predicted from model m at the i^{th} period within a discrete grid of N periods, and D^{obs} and σ are the observed compliance function and associated uncertainty-squared. The $p(m)$ is the Ps delay time predicted from model m, and the S^{obs} and δ are the measured Ps delay and associated uncertainty-squared. κ is a weighting parameter that balances the contribution of compliance and Ps delay in the joint misfit function $S_{joint}(m)$.

3.3.2. Model Parameterization and Prior Distribution Determination

At each OBS station, the S-wave velocity model includes a gradient sediment layer, defined by S-wave speeds at the top and bottom of the layer with linear variation between them, and a crustal layer defined with 4 cubic B-splines to a varying depth depending on water depth, as discussed in the next paragraph. The 1-D depth model is parameterized using S-wave velocity as seafloor compliance is most sensitive to the sub-seafloor shear modulus (Crawford et al., 1991). For the crustal layer, the P-wave velocity is derived from the S-wave velocity using the empirical relationship of Brocher (2005). In the sediment layer, the P-wave and S-wave velocities are inverted independently when Ps delay measurements are available. Otherwise, P-wave velocity is determined using the empirical relationship of Castagna et al. (1985). The density is assigned constant values: 2.0 g/cm^3 for the sediments, 2.8 g/cm^3 for the crust. In our study, we primarily sourced sediment thickness references from GlobSed (Straume et al., 2019) and seismic reflection data (Clarke et al., 2024). The values derived from these sources guide the scope of our inversion analysis, though the Bayesian inversion is only weakly affected by initial values. We assume that the sediment thicknesses derived from seismic reflection surveys is more reliable than those from GlobSed, and thereby permit a narrower perturbation range for these specific stations during the inversion. We also make iterative adjustments to the sediment thickness values based on the results from the posterior distribution. See Table S3 in Supporting Information S1 for more details.

Given that the depth-sensitivity of the compliance function to S-wave velocity is not only frequency dependent but is also depends on the water depth (Figures 4b and 4f), we set the model depth based on varying water depths: with a total thickness of 3 km assigned for stations with water depth less than 2 km, and a total thickness of 5 km assigned for stations with water depth greater than 2 km.

Finally, we impose several prior constraints: (a) $0 \le V_s \le 4.5$ km/s throughout the model. (b) V_p and V_s in the sediment layer both increase with depth monotonically, and no negative gradient of Vs in the crystalline layer is allowed. (c) The V_s jump at the sediment-crust discontinuity must be positive as depth increases. (d) $1.70 \le V_p/V_s \le 15.0$ and $V_p \le 4.0$ km/s for the sediment layer. We find that these constraints occasionally result in inadequate sampling of the model space, particularly affecting the fitting of Ps delay measurements. However, the application of these constraints is essential to maintain the reliability of our estimates and to prevent physically unrealistic models.

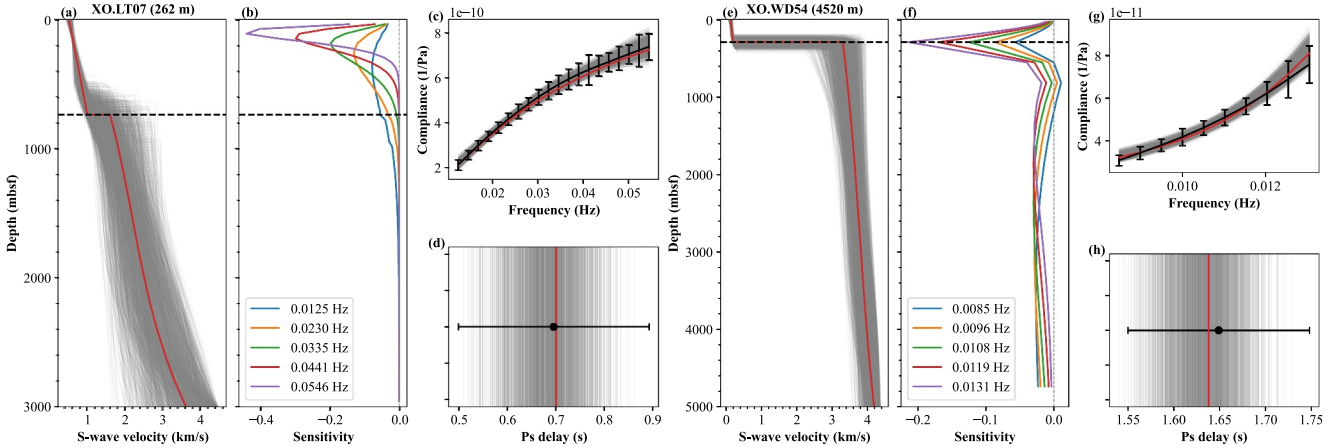

Figure 4. Inversion example at stations LT07 and WD54, positioned on the landward and oceanward sides of the trench, respectively. (a) 2,000 randomly picked Vs models (gray lines) and misfit-weighted average Vs model (red line). (b) The associated sensitivity kernel curves of seafloor compliance to S-wave velocity at select frequencies. In (a) and (b), the *y*-axis refers to the depth in meters below the seabed and the horizontal dashed line marks the estimated sediment thickness. (c) The measured compliance is delineated by the black line with error bars. Theoretical compliance, calculated from the models in (a) is shown with gray lines, with the red line being the compliance of the average model. (d) Similar to (c), but for Ps delay. Panels (a)–(d) correspond to station LT07, while panels (e)–(h) relate to station WD54.

3.3.3. Sampling Strategies and Posterior Distribution Determination

We use the No-U-Turn Sampler (Hoffman & Gelman, 2014) sampling algorithm to model space, drawing samples from posterior distributions to generate estimated quantities. Multiple sampling chains are used to improve the reliability of the posterior estimates. Within each individual chain, a "burn-in" strategy (Gilks & Roberts, 1996) is taken to discard initial samples, aimed at ensuring that the chain has reached a steady state to be representative of the target distribution. In most cases of our study, 10 chains with 20,000 draws and a burn of 10,000 are sufficient to yield reliable and robust estimates.

We calculate the root mean square (RMS) misfit function $\chi = \sqrt{\frac{S(m)}{N}}$ and follow the selection criterion as described by Shen et al. (2013) to obtain an enhanced posterior distribution. When only compliance measurements are available, we define the threshold of acceptance χ^{crit} for the seafloor compliance inversion as follows:

$$\chi^{crit} = \begin{cases} 2\chi_{min}^{comply} & if\ \chi_{min}^{comply} \geq 0.5 \\ \chi_{min}^{comply} + 0.5 & if\ \chi_{min}^{comply} < 0.5 \end{cases} \tag{8}$$

Otherwise, we calculate the RMS misfit for both compliance function (χ^{comply}) and Ps delay (χ^{Ps}), and the joint normalized relative RMS misfit function χ^{joint} is defined as follows:

$$\chi^{joint} = \frac{1}{2}\left(\frac{\chi^{comply} - \chi_{min}^{comply}}{\chi_{max}^{comply} - \chi_{min}^{comply}} + \frac{\chi^{Ps} - \chi_{min}^{Ps}}{\chi_{max}^{Ps} - \chi_{min}^{Ps}}\right) \tag{9}$$

The χ_{min}^{comply} and χ_{max}^{comply} are the minimum and maximum value of χ^{comply} for all models visited during sampling, as are Ps delays, and the criterion for model acceptance is $\chi^{joint} < \chi^{crit}$, where $\chi^{crit} = \chi_{min}^{joint} + 0.5$. Figure 4 shows an inversion example at stations LT07 and WD54, with associated prior and enhanced posterior distributions of model parameters shown in Figure 5. The final model is estimated by calculating the weighted average of the accepted model ensembles. The weight of each model is defined as Equation 10, allowing models with lower misfits to contribute more significantly to the average.

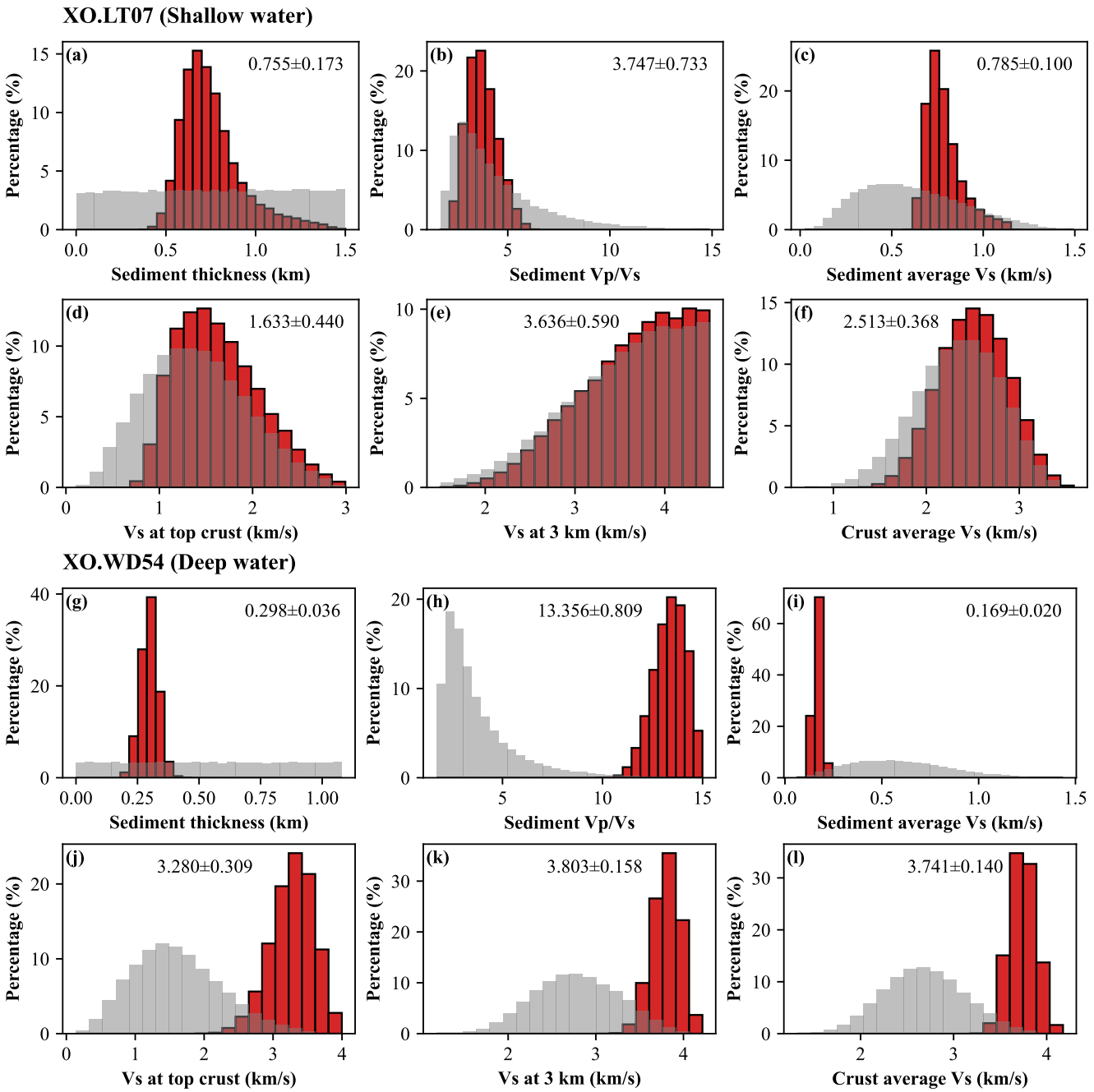

Figure 5. The prior (gray) and posterior (red) distributions of model parameters at stations LT07 and WD54. (a) Sediment thickness. (b) The derived Vp/Vs ratio for the sediment layer. (c) Depth-averaged Vs of the sediments. (d) Vs at top of crust. (e) Vs at 3.0 km depth. (f) Depth-averaged Vs in crust. Panels (a)–(f) are for station LT07, while panels (g)–(l) are for station WD54.

$$w_i = \begin{cases} \dfrac{1}{\chi_i} & \chi_i \le 1 \\ e^{1-\chi_i} & \chi_i > 1 \end{cases} \qquad (10)$$

$$w_i^{norm} = \frac{w_i}{\sum_{i=1}^{n} w_i}$$

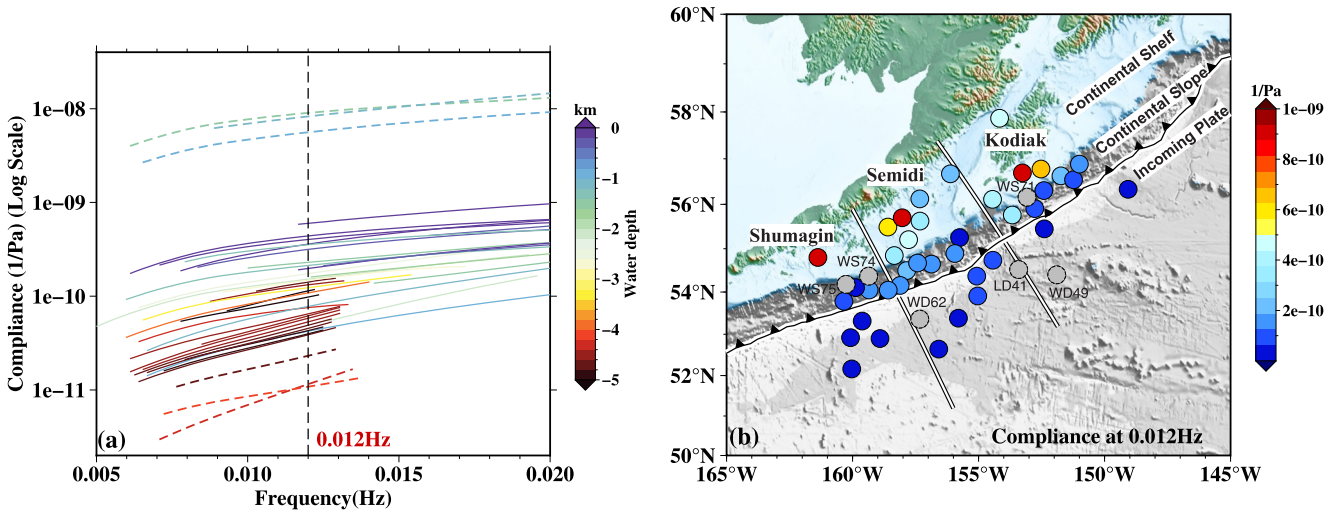

Figure 6. (a) Measured compliance as a function of frequency, with colors indicating the water depth. The dashed curves indicate the compliance measurements that failed in the S-wave velocity inversion. (b) The map of measured compliance at the frequency of 0.012 Hz (black dashed vertical line shown in (a)). The gray circles represent the stations with potential issues, dashed lines in panel (a). The white lines denote the approximate boundaries between the Shumagin, Semidi, and Kodiak segments.

4. Results

4.1. Seafloor Compliance and Ps Delay Measurements

Figure 6 presents the measured seafloor compliance at 45 stations. The compliance amplitudes measured in deep (>2000 m) and shallow (≤2000 m) water depth differ by about an order of magnitude, which suggests a stiffer seafloor for greater water depth. We observe both low and high anomaly values at 6 DPG stations (dashed lines in Figure 6a). These compliance amplitudes have been corrected through the DPG gain calibration. The stations exhibiting high compliance anomalies (WS71, WS74, WS75) produce 1-D models with extremely low S-wave velocity within the sediment and crust (~0.3 km/s), deviating significantly from empirical knowledge about the Earth's sub-seafloor (e.g., Crust 1.0 (Laske et al., 2013)). In contrast, the stations with low-value anomalies (LD41, WD49, WD62) tend to yield extremely high S-wave velocity and hence always fail to fit the measured compliance data as our inversions introduce the prior assumption that S-wave velocity values do not exceed 4.5 km/s. To fit such low compliance amplitudes ($\sim 10^{-11}$) would require an average S-wave velocities exceeding 5 km/s, which is physically questionable, even considering that these lie in a seamount area (Figure 1). The underlying causes of these measurement anomalies warrant further investigation, but here we exclude these stations for the sub-seafloor structure analysis.

The Ps delay times and associated uncertainties measured at 45 stations are shown in Figure 7. The stations with large Ps delay (≥1.0 s), indicating either high-Vp/Vs or thick sediments, are mainly located in the continental slope and on the incoming plate. We find that the uncertainties for Ps measurements for stations at shallow water depths, including the shallow continental shelf and continental slope, are typically larger than those on the incoming plate (Figure 7b). This increase in Ps measurement uncertainty principally arises from large uncertainties in the arrival times measuring on horizontal components, or the inability to make a measurement. For the OBS stations in the shallow shelf (green cubes in Figure 1a), even though equipped with trawl-resistant mounts, they may still be susceptible to high-frequency noise (>1 Hz) from vibrations or the rocking of the shield under ocean currents (Webb & Barclay, 2023). Identifying specific causes that contribute to this spatial pattern in measurement uncertainties requires further investigation, which is beyond the scope of this manuscript.

4.2. Sub-Seafloor S-Wave Velocity Model

4.2.1. Model Overview

The AACSE array spans the shallow continental shelf, continental slope, and incoming plate of the Alaska Peninsula subduction zone, and the sediment thickness across the array varies considerably, ranging from about 50 m to 2.80 km, with the thickest sediment located on the continental slope (Figures 8a and 9d). The thinnest

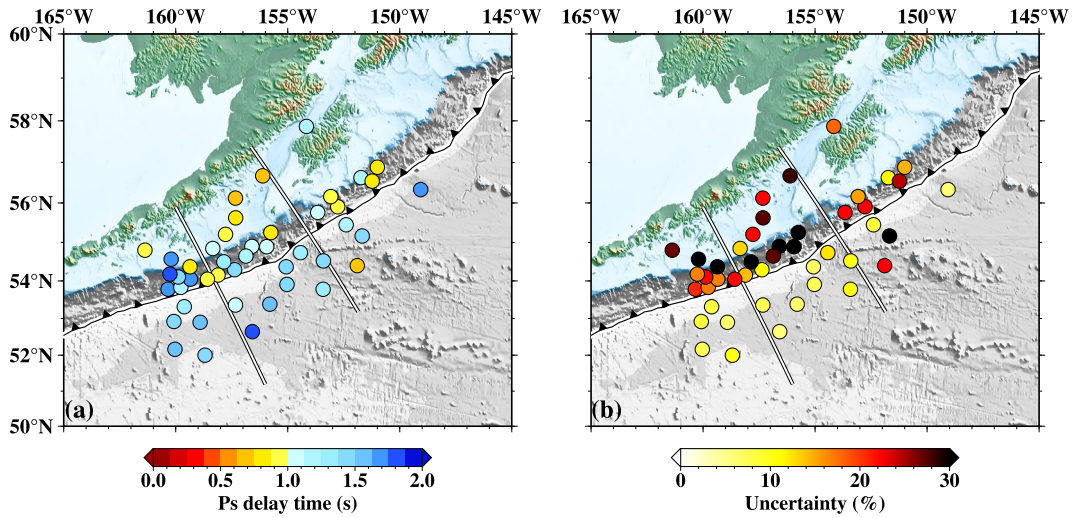

Figure 7. (a) Map of measured Ps delay times and (b) associated uncertainties. The white lines denote the approximate boundaries between the Shumagin, Semidi, and Kodiak segments.

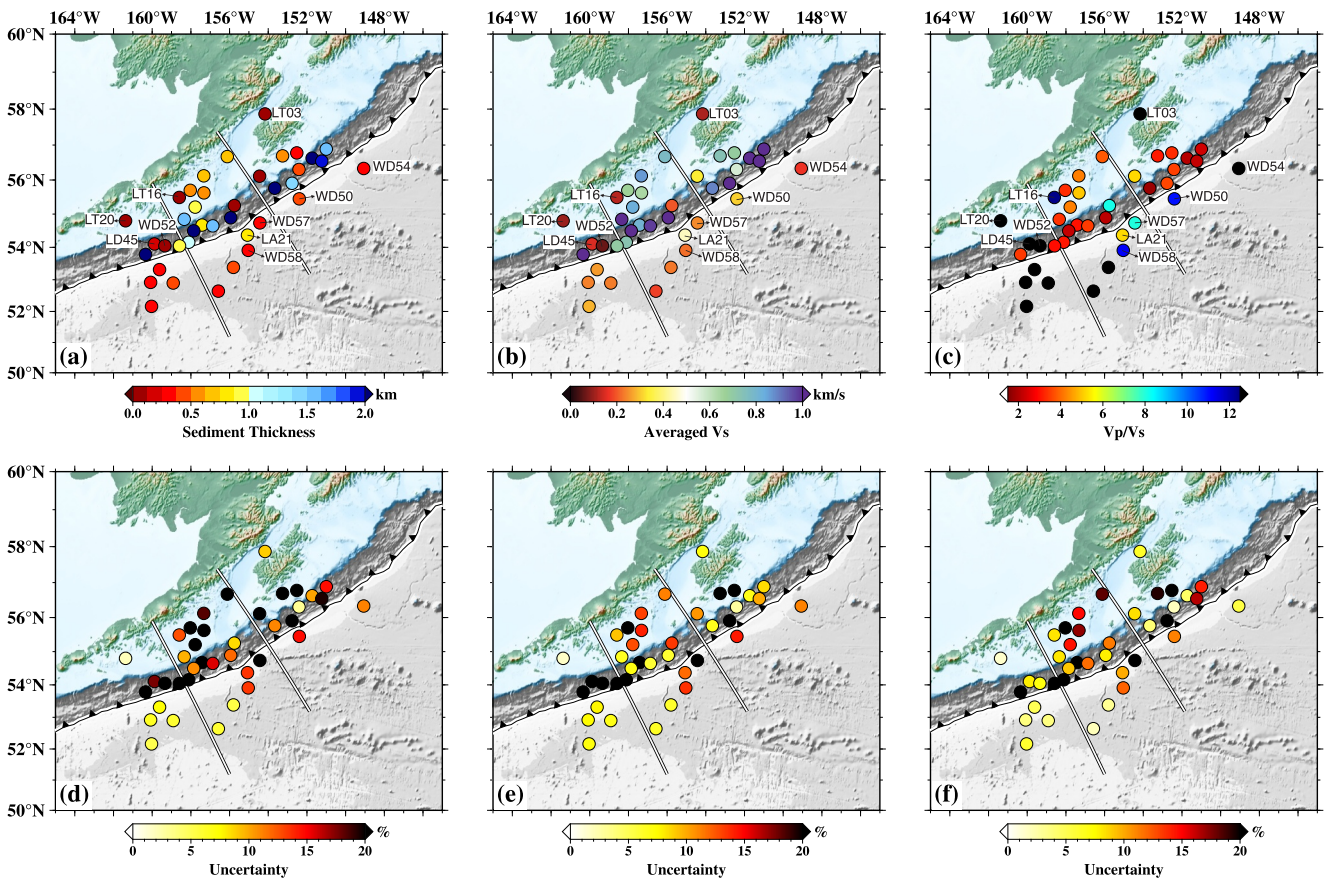

Figure 8. Map of (a) sediment thickness, (b) depth-averaged Vs in the sediments and (c) derived Vp/Vs in the sediments, estimated from the mean of the posterior distribution below each station. (d)–(f) Their associated uncertainties. The white lines denote the approximate boundaries between the Shumagin, Semidi, and Kodiak segments.

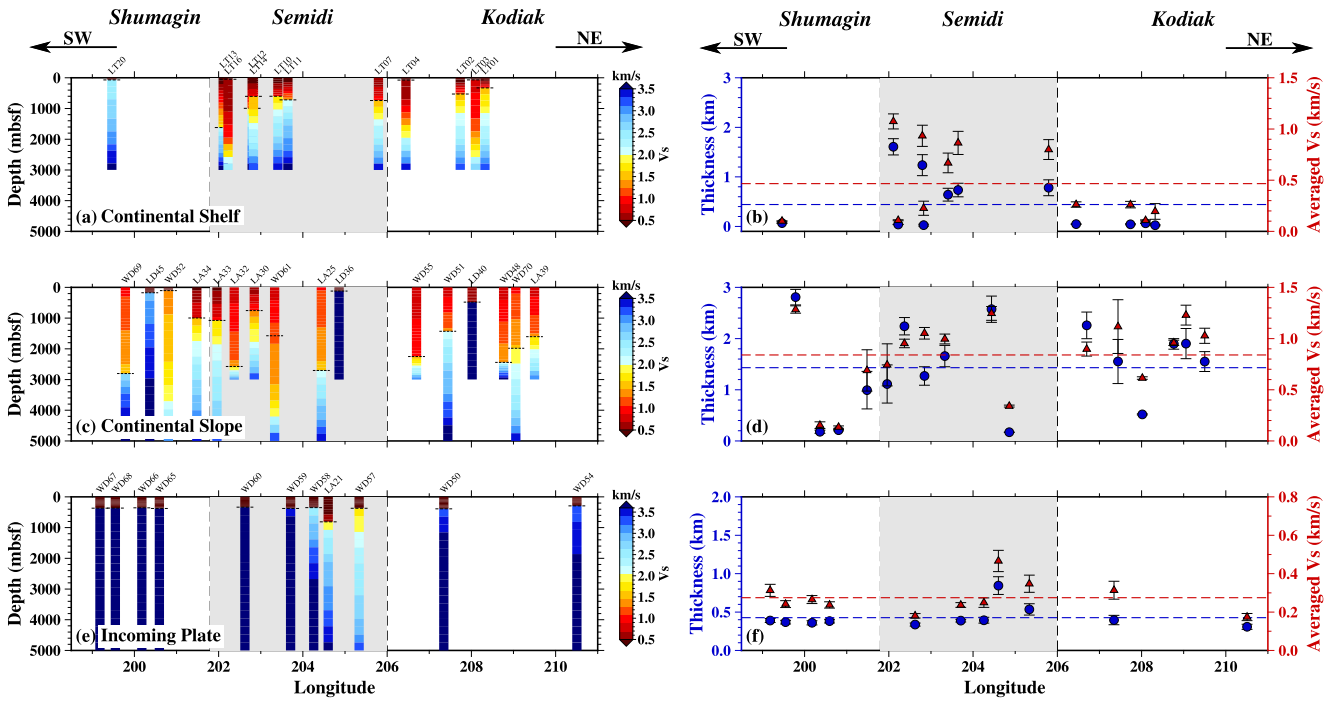

Figure 9. The 1-D crustal S-wave velocities (left panels), as well as sediment thickness and depth-averaged Vs of the sediments beneath each station (right panels), shown along strike, and taken from the mean of the posterior distribution. (a)–(b) Continental shelf. (c)–(d) Continental slope. (e)–(f) Incoming plate. The horizontal dashed lines in (a), (c), and (e) represent the estimated sediment thickness. The blue and red dashed lines in (b), (d), and (f) denote the average sediment thickness and sediment Vs within the continental shelf, continental slope, and incoming plate, respectively.

sediments, along with low Vs, occur at the stations in very shallow water (~150 m) within the shallow shelf (Figure 8a). However, these stations (LT03, LT16, and LT20), located in shallow water, do not have sufficient Ps delay measurements, which results in a deficiency of robust restrictions on the sediment thickness. The potential misestimation of sediment thickness could further lead to inaccuracies in estimating other seismic properties. Due to their substantial deviation from the reference sediment thickness and other nearby stations, we will not discuss this further. In the incoming plate, the seafloor sediment is typically thin (~0.4 km) with lower Vs (<0.4 km/s). There are a few exceptions to this pattern such as station WD57 and LA21, which have relatively thick sediment and high Vs values, are located in the Semidi segment near the trench (Figures 8a, 9f and 10d).

In addition to direct estimates of sediment thickness and depth-averaged Vs, we also derive the depth-averaged Vp/Vs ratio of seafloor sediment (Figures 8c and 8f). The estimation of Vp/Vs at the stations without valid Ps delay measurements may be subject to high inaccuracies, as the empirical scaling relationship used to determine Vp could cause errors. Yet, a general pattern emerges where the Vp/Vs ratio of the incoming sediment in deep-water areas is mostly much higher than that found on the continental shelf and slope. This correlation between higher Vp/Vs ratios and deeper water has also been reported in other oceanic regions such as offshore Cascadia (Zhu et al., 2020). There are also several exceptions including the extremely high Vp/Vs ratios at stations LD45 and WD52 within the continental slope and at stations LT03, LT16, and LT20 within the shallow shelf, as well as reduced Vp/Vs ratios at stations LA21 and WD57 near the trench within the incoming plate.

Figures 9 and 10 show the 1-D depth-velocity profile beneath 39 OBS stations along strike and dip, respectively. The spatial extent of the continental shelf, continental slope, and incoming plate are shown in Figure S4 in Supporting Information S1. Significant variability of S-wave velocities for the continental slope is observed (Figures 10c and 10d), even between closely located stations. In contrast, the S-wave velocity structure in the shallow shelf and incoming plate exhibits more uniform characteristics: the shallow shelf displays a smooth increase in velocity with depth (except station LT20), and the incoming plate seismic structure typically has a combination of low-velocity sediment and high-velocity crust. For each obtained velocity model, we calculate the corresponding compliance sensitivity kernels with respect to S-wave velocity. The compliance sensitivity kernels

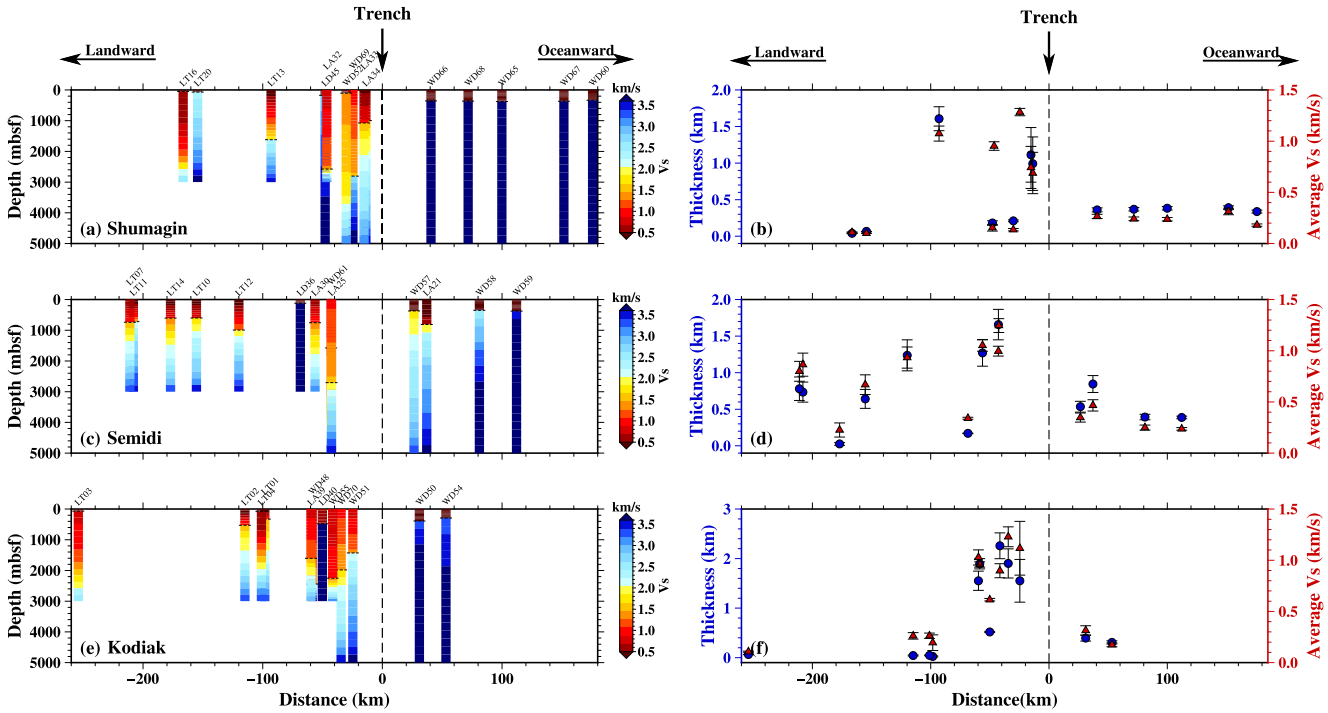

Figure 10. The 1-D S-wave velocities, as well as sediment thickness and depth-averaged Vs of seafloor sediment beneath each station, showing along dip. (a)–(b) Shumagin segment. (c)–(d) Semidi segment. (e)–(f) Kodiak segment.

(Figures 4b and 4f), along with the comparison between prior and posterior distributions (Figure 5), indicate that our inversion effectively constrains the sediment S-wave velocities, whereas it provides a certain constraint on crystalline structure only at stations in deep water.

4.2.2. Comparative Analysis

We compare the sediment thickness (Figure S6 in Supporting Information S1) and depth-averaged Vs (Figure S7 in Supporting Information S1) from this study with GlobSed (Straume et al., 2019), seismic reflection data (Clarke et al., 2024), and surface wave imaging (Li et al., 2024). We also present the comparison of 1-D depth-Vs profiles to Li et al. (2024) at several specific stations within the continental shelf, continental slope, and incoming plate (Figure S8 in Supporting Information S1).

For sediment thickness, our estimates are consistently lower than those from seismic reflection data (available only for stations on the incoming plate) and surface wave imaging. Compared with GlobSed, our results show lower values at stations on the incoming plate and varied values on the continental shelf and slope, with the largest discrepancies observed on the continental slope. In terms of sediment averaged Vs, our values are uniformly lower than those from surface wave imaging, especially for stations on the incoming plate, where differences exceed threefold.

The discrepancies observed may stem from several factors: (a) There are differences in defining the sediment layer, particularly in methods used to derive sediment properties. For instance, seismic reflection/refraction primarily estimates sediment thickness based on P-wave velocity, often using time-depth conversion with an assumed average velocity of 1.8 km/s (e.g., Clarke et al. (2024); Bécel et al. (2017)), which differs from those that rely on S-wave velocity, such as this study or surface wave imaging. (b) There is the potential to overestimate sediment Vs due to the absence of short-period dispersion data in surface wave imaging. The extraction of robust short-period (<10 s) Rayleigh wave dispersion remains a challenging task. For example, in Li et al. (2024), reliable measurements of Rayleigh phase and group velocities mostly range from 8 to 36 s, which may not provide sufficient constraints on the shallow seismic structure. In addition, relying solely on surface wave dispersion data

cannot resolve seismic discontinuities such as the sediment–crust interface, which potentially introduces additional uncertainties.

Nevertheless, we admit that while we incorporate Ps delay times into the compliance inversion, the Ps delay itself is related to both sediment thickness and the Vp/Vs (Equation 5) ratio and thus possesses inherent trade-offs. Additionally, some stations lack Ps delay measurements. These discrepancies underscore the complexity of accurately modeling sub-seafloor structure across different geophysical methods and highlight the need for integrated approaches to refine understanding of marine seismic structures.

5. Discussion

5.1. Seismic Properties of Seafloor Sediments Along the Alaska Peninsula

5.1.1. Sources and Characteristics of Seafloor Sediments in the Alaska Peninsula

The seafloor sediments near the Alaska Peninsula, particularly near the landward side of the Alaska-Aleutian trench, primarily originate from land-based sources. Along the southern coast of the peninsula, marine deposits are influenced by the southwest-flowing Alaskan Stream, which interacts with coastal islands and extends across shallow shelves up to 120 km offshore (Zimmermann et al., 2019). The geological composition of most of the peninsula includes Mesozoic turbiditic sedimentary rocks, as well as volcanic and other sedimentary rocks from the Cretaceous to the Quaternary periods (Detterman et al., 1996; Vallier et al., 1994). Over the past about 200 million years, the region has experienced considerable geological changes, including significant uplift, volcanic activities and glaciation.

On the oceanward side of the trench, the main sediment input (Figure 1c) comes from the Zodiac Fan (Stevenson et al., 1983) and Surveyor Fan (Reece et al., 2011), which surround the seamounts such as the Patton Murray Seamount (Figure 1a). Most of sediments in this region were carried by turbidity currents from continental sources (Hamilton, 1967) and they accumulate at high sedimentation rates (Chaytor et al., 2007). A portion of these sediments reach the seamount areas, which are habitats for diverse deep-sea fauna and thus contribute to extensive deposition of biogenic materials (Gartman et al., 2022).

Lithologically (Figure 1c, Dutkiewicz et al. (2015)), the clay-rich sediments dominate the continental shelf and slope on the landward side of the trench. In contrast, the sediments on the incoming plate exhibit a more varied composition, including the clay near the trench as well as the sand and siliceous mud in the abyssal plains. The areas around seamounts feature a complex assemblage of sediment compositions, notably characterized by substantial biogenic deposits. Seafloor sediments within incoming plate in deeper waters are subjected to higher hydrostatic pressure, which typically leads to increased compaction and decreased porosity. This condition is expected to increase S-wave velocities compared to those in shallower waters. Nevertheless, our findings challenge this expectation, indicating something besides merely water depth affects the seismic properties of seafloor sediments in this region. In the incoming plate, a distinct variation in Vs and Vp/Vs between locations near the trench (the stations LA21, WD57, and WD50) and those in the abyssal plains and seamount areas is observed (Figure 8). Sediments near the trench tend to contain a significant amount of clay, whereas those in the abyssal plains and seamounts are characterized by complex deep-sea depositional environments, including notable contributions from biogenic deposits (Figure 1c). These observations suggest that local differences in the seismic velocities of sediments may be closely related to their lithological composition. In areas with complex deep-sea depositional sequences, we typically observe lower Vs and higher Vp/Vs ratios, whereas sediments with a higher clay content display the reverse pattern.

5.1.2. Impact of Seafloor Sediment on Surface Wave Propagation and Characteristics

The marine environment allows the occurrence of various types of surface waves such as Scholte waves and Rayleigh waves, which occur for both fundamental and higher modes (overtones). Scholte waves, propagating at the water-seabed interface, have been observed in both active- (e.g., Wang et al. (2016)) and passive-source (e.g., Williams et al. (2021)) data and are widely used for to characterize seabed sediments. Observation and utilization of Rayleigh wave overtones are also extensively reported, the occurrence of which is also closely related to seafloor sediments (Bowden et al., 2016; Takagi & Nishida, 2022). The fundamental-mode Rayleigh wave serves as a crucial tool to image the structure of the deeper crust and mantle, although some studies report that seafloor sediments can capture and trap high-frequency energy from fundamental-mode Rayleigh

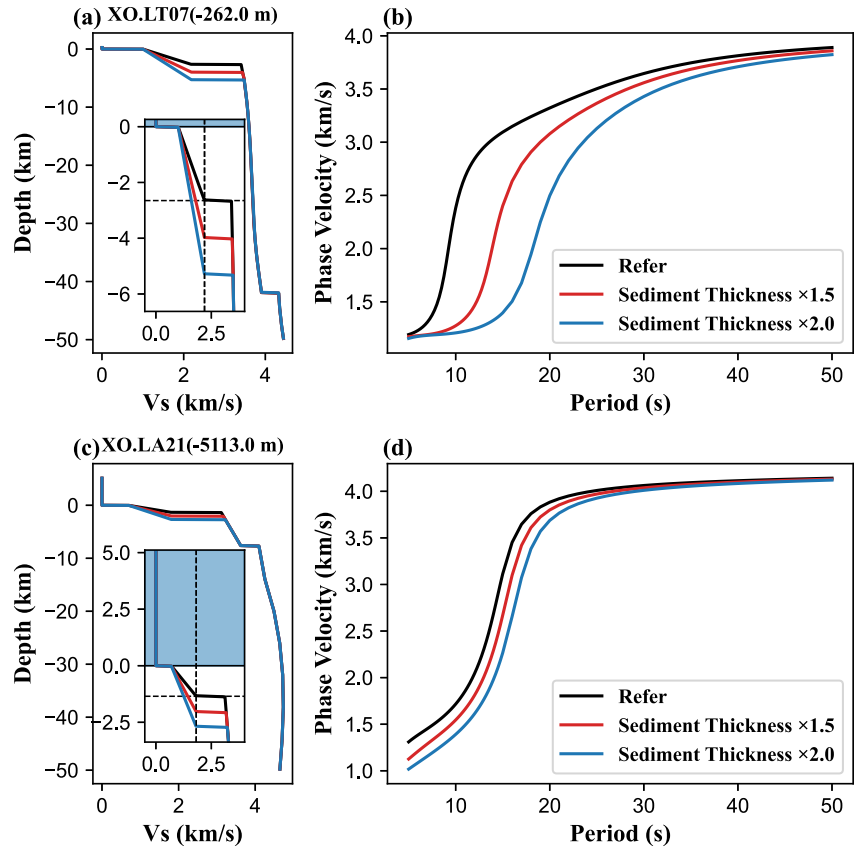

Figure 11. Impact of sediment thickness perturbations on fundamental-mode Rayleigh wave dispersion. (a) 1-D Vs profile beneath station LT07, with an inset zooming in on the seafloor sediment. Different line colors correspond to thickness perturbations to the sediment layer as explained in the legend of (b). The positive and negative ranges of the *y*-axis represent water depth and the depth beneath the seabed, with the water layer filled with light blue. The horizontal dashed line in the zoom-in figure marks the bottom of the sediment layer, and the vertical dashed line is the Vs at the bottom of the sediment layer. (b) The corresponding Rayleigh wave phase velocity dispersion from 8 to 50 s. Panels (c)–(d) replicate this setup for station LA21 in deeper water.

waves. For example, Tian et al. (2013) identified two highly dispersed wave phases in ambient noise cross-correlations using the Cascadia Initiative OBS data and attributed the short-period and long-period signals to the water-sediment and crust-mantle waveguides, respectively. Similar phenomena also occur in the noise cross-correlations of AACSE data (Figure S10 in Supporting Information S1, Liu et al. (2022)).

While the short-period surface wave dispersion (<10 s) induced by seafloor sediments is challenging to measure robustly in marine seismic data, the presence of sediments may affect the measurements of longer period dispersion. Neglecting or inaccurately estimating the sediment structure can adversely affect the characterization of the underlying deeper structure. To investigate this, we examine stations LT07 and LA21 (Figure 1), located in shallow and deep water, respectively, to see how fundamental-mode Rayleigh wave dispersion changes if we overestimate the sediment thickness. The 1-D S-wave velocities for these stations, encompassing the seafloor sediment and underlying oceanic crust and mantle, are extracted from Li et al. (2024), other seismic properties are simply assigned with constant (Vp of 1.8, 7.0, and 8.0 km/s and density of 2.0, 2.8, and 3.0 g/cm^3 for the sediment, crust, and mantle, respectively). We model the S-wave velocities within the sediment as a gradient layer, keeping the Vs at the top and bottom constant, in order to ensure that the average Vs of the sediment layer does not change when the sediment thickness varies.

Our analysis suggests (Figure 11) that variations in sediment thickness substantially alter the dispersion curves at periods less than 30 s, both for stations in shallow and deep water, although the effect is smaller in deep water. Consequently, if sediment properties are not properly addressed, the measured dispersion may be misinterpreted

or shallow anomalies may be attributed to greater depths. This emphasizes the importance of accounting for the effects of sediments in marine surface wave seismic imaging. Failing to do so may lead to errors in the estimates of S-wave velocities of deeper structures.

5.2. Seismic Structure of Shallow Oceanic Crust: Ties to Seafloor Spreading History

The Pacific oceanic crust involved in our study area formed in the late Tertiary (48–56 Ma), which subsequently has undergone the reorganization of the old Pacific plate, including a reorientation of the Kula ridge and a shift in the Kula–Pacific–Farallon triple junction (Lonsdale, 1988; Seton et al., 2012). The fossil triple junction resulting from the reorganization is situated at the T-shaped magnetic anomaly (blue dashed line in Figure 1b). Due to this reorganization, the regional oceanic crust has experienced significant variations in the direction and rate of spreading during this period (Figure 1b), with Pacific–Kula fast spreading in the west (74 mm/yr half-rate, Engebretson et al. (1984); 54 mm/yr half-rate, Lonsdale (1988)) and Pacific–Farallon intermediate spreading in the east (~28–34 mm/yr half-rate, Engebretson et al. (1984)).

Differences in spreading rate or style, such as shifting from magma-dominated to tectonism-dominated, or a change in orientation, can result in differences in oceanic crust structure (Peirce & Hobbs, 2024). For example, oceanic crust formed at slower spreading rates often exhibits more faults and fractures and associated lower seismic velocities. In addition, the lithological structure within the crust varies with spreading rate: fast-spreading crust with ample magma supply typically has a shallow dike-gabbro boundary with a thicker lower crustal gabbroic section; the opposite is true for slower spreading rates (Christeson et al., 2019). In our study area, away from the trench, active-source seismic imaging (Bécel et al., 2015) identifies smoother seafloor topography, thinner sediment cover with less faulting, and a thicker igneous section in the Shumagin segment formed at fast spreading rates, contrasting with the Semidi segment formed at intermediate spreading rates. However, while it extends to the incoming plate near the trench (<100 km), the Shumagin segment tends to have many more outer-rise plate bending faults than the Semidi segment (Clarke et al., 2024). Our sub-seafloor model, based on sampling of the adjacent areas in the fossil triple junction, reveals that the S-wave velocities of the upper crust on the Semidi incoming plate are lower than those on the Shumagin segment (Figures 9e and 10a–10c). This finding aligns with previous observations and might provide evidence from the perspective of seismic S-wave velocities for different spreading rates between the Semidi and Shumagin segments. The lower S-wave velocities within Semidi segment could be attributed to earlier intermediate spreading, which resulted in increased faulting and possible lithological variations.

6. Conclusions

We use seafloor compliance and Ps delay times measured from the AACSE OBS data to image the marine sediment and shallow crust across the Alaska-Aleutian subduction zone offshore of the Alaska Peninsula. The sediment thickness varies from about 50 m to 2.80 km across the array, with the thickest sediment located in the continental slope. Lower Vs and high Vp/Vs ratios characterize the deep-sea depositional sediments of the incoming plate, differing from the clay-rich sediments of the continental shelf and slope. Exceptions to this pattern also occur, suggesting that variations in lithology lead to local anomalies in the seismic properties of marine sediments. We observe the difference in S-wave velocity of the upper oceanic crust formed at fast (Shumagin) and intermediate (Semidi) spreading rates and attribute the reduced S-wave velocities of the Semidi upper crust to increased faulting and possible lithological variations associated with lower-rate spreading.

Data Availability Statement

The facilities of EarthScope Consortium Data Services were used for access to waveforms and related metadata from AACSE XO network (Abers et al., 2018; Barcheck et al., 2020). The OBStools for processing ocean-bottom seismic data and measuring seafloor compliance can be accessed at Audet and Janiszewski (2022). The disba (Luu, 2021) is used for computing theoretical Rayleigh wave dispersions. The code for computing compliance sensitivity kernels and compliance Monte-Carlo inversion can be requested from the corresponding author or be found at Zheng (2024). The sub-seafloor seismic model presented herein is available at Zheng et al. (2024).

Acknowledgments
We thank the reviewers, associate editor Colin Farquharson, and editor Fenglin Niu for their constructive and insightful comments. We are highly grateful to all the field teams involved in collecting the AACSE data, with special thanks to the other PIs: Geoffrey Abers, Aubreya Adams, Emily Roland, Susan Schwartz, Spahr Webb, and Lindsay Worthington. We also appreciate the dedicated efforts of the ship captains and crew members, as well as the OBS engineers from Woods Hole and Lamont-Doherty. We thank Drs. Justin Ball, Simon Rebeyrol, Pascal Audet, Helen Janiszewski, Yang Zha and Gabi Laske for helpful discussions and suggestions. We also thank Drs. Wayne Crawford and Stephen Mosher for generously providing their compliance forward packages. We thank Drs. Donna Shillington and Zongsan Li for sharing the seismic models from their studies. This study was funded by NSF Grants OCE-1952209 and RISE-1855090 at the University of Colorado Boulder.

References

Abers, G., Wiens, D., Schwartz, S., Sheehan, A., Shillington, D., Worthington, L., et al. (2018). AACSE: Alaska amphibious community seismic experiment [Dataset]. *International Federation of Digital Seismograph Networks*. https://doi.org/10.7914/SN/XO_2018

Abers, G. A. (1992). Relationship between shallow- and intermediate-depth seismicity in the eastern Aleutian subduction zone. *Geophysical Research Letters*, *19*(20), 2019–2022. https://doi.org/10.1029/92GL02060

Agius, M. R., Harmon, N., Rychert, C. A., Tharimena, S., & Kendall, J. M. (2018). Sediment characterization at the equatorial mid-atlantic ridge from P-to-S teleseismic phase conversions recorded on the PI-LAB experiment. *Geophysical Research Letters*, *45*(22), 12244–212252. https://doi.org/10.1029/2018GL080565

Alibés, B., Rothwell, R. G., Canals, M., Weaver, P. P. E., & Alonso, B. (1999). Determination of sediment volumes, accumulation rates and turbidite emplacement frequencies on the Madeira abyssal plain (NE atlantic): A correlation between seismic and borehole data. *Marine Geology*, *160*(3), 225–250. https://doi.org/10.1016/S0025-3227(99)00026-2

Audet, P. (2016). Receiver functions using OBS data: Promises and limitations from numerical modelling and examples from the Cascadia initiative. *Geophysical Journal International*, *205*(3), 1740–1755. https://doi.org/10.1093/gji/ggw111

Audet, P., & Janiszewski, H. (2022). OBStools: Software for processing broadband ocean-bottom seismic data (Version v0.1.3) [Software]. *Zenodo*. https://doi.org/10.5281/zenodo.6491249

Ball, J. S., Sheehan, A. F., Stachnik, J. C., Lin, F.-C., & Collins, J. A. (2014). A joint Monte Carlo analysis of seafloor compliance, Rayleigh wave dispersion and receiver functions at ocean bottom seismic stations offshore New Zealand. *Geochemistry, Geophysics, Geosystems*, *15*(12), 5051–5068. https://doi.org/10.1002/2014GC005412

Barcheck, G., Abers, G. A., Adams, A. N., Bécel, A., Collins, J., Gaherty, J. B., et al. (2020). The Alaska amphibious community seismic experiment. *Seismological Research Letters*, *91*(6), 3054–3063. https://doi.org/10.1785/0220200189

Bécel, A., Shillington, D. J., Delescluse, M., Nedimović, M. R., Abers, G. A., Saffer, D. M., et al. (2017). Tsunamigenic structures in a creeping section of the Alaska subduction zone. *Nature Geoscience*, *10*(8), 609–613. https://doi.org/10.1038/ngeo2990

Bécel, A., Shillington, D. J., Nedimović, M. R., Webb, S. C., & Kuehn, H. (2015). Origin of dipping structures in fast-spreading oceanic lower crust offshore Alaska imaged by multichannel seismic data. *Earth and Planetary Science Letters*, *424*, 26–37. https://doi.org/10.1016/j.epsl.2015.05.016

Bell, S. W., Ruan, Y., & Forsyth, D. W. (2015). Shear velocity structure of abyssal plain sediments in Cascadia. *Seismological Research Letters*, *86*(5), 1247–1252. https://doi.org/10.1785/0220150101

Bilek, S. L., & Lay, T. (2018). Subduction zone megathrust earthquakes. *Geosphere*, *14*(4), 1468–1500. https://doi.org/10.1130/GES01608.1

Bowden, D. C., Kohler, M. D., Tsai, V. C., & Weeraratne, D. S. (2016). Offshore Southern California lithospheric velocity structure from noise cross-correlation functions. *Journal of Geophysical Research: Solid Earth*, *121*(5), 3415–3427. https://doi.org/10.1002/2016JB012919

Brizzi, S., van Zelst, I., Funiciello, F., Corbi, F., & van Dinther, Y. (2020). How sediment thickness influences subduction dynamics and seismicity. *Journal of Geophysical Research: Solid Earth*, *125*(8), e2019JB018964. https://doi.org/10.1029/2019JB018964

Brocher, T. M. (2005). Empirical relations between elastic wavespeeds and density in the Earth's crust. *Bulletin of the Seismological Society of America*, *95*(6), 2081–2092. https://doi.org/10.1785/0120050077

Brocher, T. M., Filson, J. R., Fuis, G. S., Haeussler, P. J., Holzer, T. L., Plafker, G., & Blair, J. L. (2014). The 1964 great Alaska earthquake and tsunamis: A modern perspective and enduring legacies (2014-3018). *Fact Sheet*. https://doi.org/10.3133/fs20143018

Cai, C., Wiens, D. A., Shen, W., & Eimer, M. (2018). Water input into the Mariana subduction zone estimated from ocean-bottom seismic data. *Nature*, *563*(7731), 389–392. https://doi.org/10.1038/s41586-018-0655-4

Castagna, J. P., Batzle, M. L., & Eastwood, R. L. (1985). Relationships between compressional-wave and shear-wave velocities in clastic silicate rocks. *Geophysics*, *50*(4), 571–581. https://doi.org/10.1190/1.1441933

Chaytor, J. D., Keller, R. A., Duncan, R. A., & Dziak, R. P. (2007). Seamount morphology in the Bowie and Cobb hot spot trails, Gulf of Alaska. *Geochemistry, Geophysics, Geosystems*, *8*(9). https://doi.org/10.1029/2007GC001712

Chichester, B., Rychert, C., Harmon, N., Allen, R., Collier, J., Henstock, T., & Rietbrock, A. (2020). Seafloor sediment thickness beneath the VoiLA broad-band ocean-bottom seismometer deployment in the Lesser Antilles from P-to-S delay times. *Geophysical Journal International*, *223*(3), 1758–1768. https://doi.org/10.1093/gji/ggaa360

Christeson, G. L., Goff, J. A., & Reece, R. S. (2019). Synthesis of oceanic crustal structure from two-dimensional seismic profiles. *Reviews of Geophysics*, *57*(2), 504–529. https://doi.org/10.1029/2019RG000641

Clarke, J., Shillington, D., Christine, R., Gaherty, J. B., Estep, J., Wiens, D. A., et al. (2024). Controls on bending-related faulting offshore of the Alaska peninsula. *Geochemistry, Geophysics, Geosystems*, *25*(3), e2023GC011271. https://doi.org/10.1029/2023GC011271

Crawford, W. C. (2004). The sensitivity of seafloor compliance measurements to sub-basalt sediments. *Geophysical Journal International*, *157*(3), 1130–1145. https://doi.org/10.1111/j.1365-246X.2004.02264.x

Crawford, W. C., & Webb, S. C. (2000). Identifying and removing tilt noise from low-frequency (<0.1 Hz) seafloor vertical seismic data. *Bulletin of the Seismological Society of America*, *90*(4), 952–963. https://doi.org/10.1785/0119990121

Crawford, W. C., Webb, S. C., & Hildebrand, J. A. (1991). Seafloor compliance observed by long-period pressure and displacement measurements. *Journal of Geophysical Research*, *96*(B10), 16151–16160. https://doi.org/10.1029/91JB01577

Crawford, W. C., Webb, S. C., & Hildebrand, J. A. (1998). Estimating shear velocities in the oceanic crust from compliance measurements by two-dimensional finite difference modeling. *Journal of Geophysical Research*, *103*(B5), 9895–9916. https://doi.org/10.1029/97JB03532

Davies, J., Sykes, L., House, L., & Jacob, K. (1981). Shumagin Seismic Gap, Alaska Peninsula: History of great earthquakes, tectonic setting, and evidence for high seismic potential. *Journal of Geophysical Research*, *86*(B5), 3821–3855. https://doi.org/10.1029/JB086iB05p03821

Detterman, R. L., Case, J. E., Miller, J. W., Wilson, F. H., & Yount, M. E. (1996). Stratigraphic framework of the Alaska peninsula (1969A). *Bulletin*. https://doi.org/10.3133/b1969A

Doran, A. K. (2019). *Imaging the oceanic crust with broadband seismic and pressure data*. University of California.

Doran, A. K., & Laske, G. (2019). Seismic structure of marine sediments and upper oceanic crust surrounding Hawaii. *Journal of Geophysical Research: Solid Earth*, *124*(2), 2038–2056. https://doi.org/10.1029/2018JB016548

Doran, A. K., Rapa, M., Laske, G., Babcock, J., & McPeak, S. (2019). Calibration of differential pressure Gauges through in situ testing. *Earth and Space Science*, *6*(12), 2663–2670. https://doi.org/10.1029/2019EA000783

Drooff, C., & Freymueller, J. T. (2021). New constraints on slip deficit on the Aleutian megathrust and inflation at Mt. Veniaminof, Alaska from repeat GPS measurements. *Geophysical Research Letters*, *48*(4), e2020GL091787. https://doi.org/10.1029/2020GL091787

Dutkiewicz, A., Müller, R. D., Callaghan, S., & Jónasson, H. (2015). Census of seafloor sediments in the world's ocean. *Geology*, *43*(9), 795–798. https://doi.org/10.1130/G36883.1

Engebretson, D. C., Cox, A., & Gordon, R. G. (1984). Relative motions between oceanic plates of the Pacific Basin. *Journal of Geophysical Research*, *89*(B12), 10291–10310. https://doi.org/10.1029/JB089iB12p10291

Francisca, F., Yun, T. S., Ruppel, C., & Santamarina, J. C. (2005). Geophysical and geotechnical properties of near-seafloor sediments in the northern Gulf of Mexico gas hydrate province. *Earth and Planetary Science Letters*, *237*(3), 924–939. https://doi.org/10.1016/j.epsl.2005.06.050

Fujie, G., Kodaira, S., Kaiho, Y., Yamamoto, Y., Takahashi, T., Miura, S., & Yamada, T. (2018). Controlling factor of incoming plate hydration at the north-western Pacific margin. *Nature Communications*, *9*(1), 3844. https://doi.org/10.1038/s41467-018-06320-z

Gartman, A., Mizell, K., & Kreiner, D. C. (2022). Marine minerals in Alaska — A review of coastal and deep-ocean regions. *Professional Paper* (1870), 46. https://doi.org/10.3133/pp1870

Gilks, W. R., & Roberts, G. O. (1996). Strategies for improving MCMC. In W. R. Gilks, S. Richardson, & D. Spiegelhalter (Eds.), *Markov chain Monte Carlo in practice* (Vol. 6, pp. 89–114).

Gomberg, J. (2018). Cascadia onshore-offshore site response, submarine sediment mobilization, and earthquake recurrence. *Journal of Geophysical Research: Solid Earth*, *123*(2), 1381–1404. https://doi.org/10.1002/2017JB014985

Guo, Z., Lin, J., Zhang, J., Zhang, F., Yang, X., Cheng, Z., & Zhou, P. (2023). The effect of pre-existing fabrics on plate bending and seismicity in Alaska subduction zone. *Terra Nova*, *36*(3), 210–216. https://doi.org/10.1111/ter.12699

Hamilton, E. L. (1967). Marine geology of abyssal plains in the Gulf of Alaska. *Journal of Geophysical Research*, *72*(16), 4189–4213. https://doi.org/10.1029/JZ072i016p04189

Harmon, N., Forsyth, D. W., Lamm, R., & Webb, S. C. (2007). P and S wave delays beneath intraplate volcanic ridges and gravity lineations near the East Pacific Rise. *Journal of Geophysical Research*, *112*(B3). https://doi.org/10.1029/2006JB004392

Hoffman, M. D., & Gelman, A. (2014). The No-U-Turn sampler: Adaptively setting path lengths in Hamiltonian Monte Carlo. *Journal of Machine Learning Research*, *15*(1), 1593–1623. https://doi.org/10.48550/arXiv.1111.4246

Janiszewski, H. A., Gaherty, J. B., Abers, G. A., Gao, H., & Eilon, Z. C. (2019). Amphibious surface-wave phase-velocity measurements of the Cascadia subduction zone. *Geophysical Journal International*, *217*(3), 1929–1948. https://doi.org/10.1093/gji/ggz051

John, S., Thomas, W., & Christopher, F. (2016). Probabilistic programming in Python using PyMC3. *PeerJ Computer Science*, *2*, e55. https://doi.org/10.7717/peerj-cs.55

Kaneko, Y., Ito, Y., Chow, B., Wallace, L. M., Tape, C., Grapenthin, R., et al. (2019). Ultra-long duration of seismic ground motion arising from a thick, low-velocity sedimentary wedge. *Journal of Geophysical Research: Solid Earth*, *124*(10), 10347–10359. https://doi.org/10.1029/2019JB017795

Kelemen, P. B., Yogodzinski, G. M., & Scholl, D. W. (2004). Along-strike variation in the Aleutian island arc: Genesis of high Mg# Andesite and implications for continental crust. In *Inside the subduction factory* (pp. 223–276).

Kim, H. J., Kawakatsu, H., Akuhara, T., Shinohara, M., Shiobara, H., Sugioka, H., & Takagi, R. (2021). Receiver function imaging of the amphibious NE Japan subduction zone—Effects of low-velocity sediment layer. *Journal of Geophysical Research: Solid Earth*, *126*(9), e2021JB021918. https://doi.org/10.1029/2021JB021918

Laske, G., Masters, G., Ma, Z., & Pasyanos, M. (2013). Update on CRUST1. 0—A 1-degree global model of Earth's crust. *Paper presented at the Geophysical research abstracts*.

Li, J., Shillington, D. J., Saffer, D. M., Bécel, A., Nedimović, M. R., Kuehn, H., et al. (2018). Connections between subducted sediment, pore-fluid pressure, and earthquake behavior along the Alaska megathrust. *Geology*, *46*(4), 299–302. https://doi.org/10.1130/G39557.1

Li, S., Freymueller, J., & McCaffrey, R. (2016). Slow slip events and time-dependent variations in locking beneath Lower Cook Inlet of the Alaska-Aleutian subduction zone. *Journal of Geophysical Research: Solid Earth*, *121*(2), 1060–1079. https://doi.org/10.1002/2015JB012491

Li, S., & Freymueller, J. T. (2018). Spatial variation of slip behavior beneath the Alaska peninsula along Alaska-Aleutian subduction zone. *Geophysical Research Letters*, *45*(8), 3453–3460. https://doi.org/10.1002/2017GL076761

Li, Z., Wiens, D. A., Shen, W., & Shillington, D. J. (2024). Along-strike variations of Alaska subduction zone structure and hydration determined from amphibious seismic data. *Journal of Geophysical Research: Solid Earth*, *129*(3), e2023JB027800. https://doi.org/10.1029/2023JB027800

Liu, C., & Ritzwoller, M. H. (2024). Seismic anisotropy and deep crustal deformation across Alaska. *Journal of Geophysical Research: Solid Earth*, *129*(5), e2023JB028525. https://doi.org/10.1029/2023JB028525

Liu, C., Sheehan, A. F., & Ritzwoller, M. H. (2024). Seismic azimuthal anisotropy beneath the Alaska subduction zone. *Geophysical Research Letters*, *51*(14), e2024GL109758. https://doi.org/10.1029/2024GL109758

Liu, C., Zhang, S., Sheehan, A. F., & Ritzwoller, M. H. (2022). Surface wave isotropic and azimuthally anisotropic dispersion across Alaska and the Alaska-Aleutian subduction zone. *Journal of Geophysical Research: Solid Earth*, *127*(11), e2022JB024885. https://doi.org/10.1029/2022JB024885

Lonsdale, P. (1988). Paleogene history of the Kula plate: Offshore evidence and onshore implications. *GSA Bulletin*, *100*(5), 733–754. https://doi.org/10.1130/0016-7606(1988)100<0733:PHOTKP>2.3.CO;2

Lopez, T., Fischer, T. P., Plank, T., Malinverno, A., Rizzo, A. L., Rasmussen, D. J., et al. (2023). Tracking carbon from subduction to outgassing along the Aleutian-Alaska volcanic arc. *Science Advances*, *9*(26), eadf3024. https://doi.org/10.1126/sciadv.adf3024

Luu, K. (2021). disba: Numba-accelerated computation of surface wave dispersion (Version v0.6.1) [Software]. *Zenodo*. https://doi.org/10.5281/zenodo.5775195

Lynner, C. (2021). Anisotropy-revealed change in hydration along the Alaska subduction zone. *Geology*, *49*(9), 1122–1125. https://doi.org/10.1130/G48860.1

Ma, S., & Nie, S. (2019). Dynamic wedge failure and along-arc variations of Tsunamigenesis in the Japan trench margin. *Geophysical Research Letters*, *46*(15), 8782–8790. https://doi.org/10.1029/2019GL083148

Madrussani, G., Rossi, G., Rebesco, M., Picotti, S., Urgeles, R., & Llopart, J. (2018). Sediment properties in submarine mass-transport deposits using seismic and rock-physics off NW Barents Sea. *Marine Geology*, *402*, 264–278. https://doi.org/10.1016/j.margeo.2017.11.013

Mosher, S. G., Eilon, Z., Janiszewski, H., & Audet, P. (2021). Probabilistic inversion of seafloor compliance for oceanic crustal shear velocity structure using mixture density neural networks. *Geophysical Journal International*, *227*(3), 1879–1892. https://doi.org/10.1093/gji/ggab315

Müller, R. D., Sdrolias, M., Gaina, C., & Roest, W. R. (2008). Age, spreading rates, and spreading asymmetry of the world's ocean crust. *Geochemistry, Geophysics, Geosystems*, *9*(4). https://doi.org/10.1029/2007GC001743

Naliboff, J. B., Billen, M. I., Gerya, T., & Saunders, J. (2013). Dynamics of outer-rise faulting in oceanic-continental subduction systems. *Geochemistry, Geophysics, Geosystems*, *14*(7), 2310–2327. https://doi.org/10.1002/ggge.20155

Nishenko, S. P., & Jacob, K. H. (1990). Seismic potential of the queen Charlotte-Alaska-Aleutian seismic zone. *Journal of Geophysical Research*, *95*(B3), 2511–2532. https://doi.org/10.1029/JB095iB03p02511

Olakunle, O. K., Ajibola, L. M., Muhammad, I. H., & Makovsky, Y. (2021). Massive seafloor mounds depict potential for seafloor mineral deposits in the Great South Basin (GSB) offshore New Zealand. *Scientific Reports*, *11*(1), 9185. https://doi.org/10.1038/s41598-021-88620-x

Peirce, C., & Hobbs, R. W. (2024). Oceanic crust—Seismic structure, lithology and the cause of the 2A event at borehole 504B. *Geophysical Journal International*, *237*(1), 159–189. https://doi.org/10.1093/gji/ggae029

Ramos, M. D., Liberty, L. M., Haeussler, P. J., & Humphreys, R. (2022). Upper-plate structure and tsunamigenic faults near the Kodiak Islands, Alaska, USA. *Geosphere*, *18*(5), 1474–1491. https://doi.org/10.1130/GES02486.1

Reece, R. S., Gulick, S. P. S., Horton, B. K., Christeson, G. L., & Worthington, L. L. (2011). Tectonic and climatic influence on the evolution of the surveyor fan and channel system, Gulf of Alaska. *Geosphere*, *7*(4), 830–844. https://doi.org/10.1130/GES00654.1

Roberts, H. H., Hardage, B. A., Shedd, W. W., & Hunt, J. (2006). Seafloor reflectivity—An important seismic property for interpreting fluid/gas expulsion geology and the presence of gas hydrate. *The Leading Edge*, *25*(5), 620–628. https://doi.org/10.1190/1.2202667

Rona, P. A. (2003). Resources of the sea floor. *Science*, *299*(5607), 673–674. https://doi.org/10.1126/science.1080679

Ruan, Y., Forsyth, D. W., & Bell, S. W. (2014). Marine sediment shear velocity structure from the ratio of displacement to pressure of Rayleigh waves at seafloor. *Journal of Geophysical Research: Solid Earth*, *119*(8), 6357–6371. https://doi.org/10.1002/2014JB011162

Ryan, H. F., von, H., Wells, R. E., Scholl, D. W., Kirby, S., & Draut, A. E. (2012). History of earthquakes and tsunamis along the eastern Aleutian-Alaska megathrust, with implications for tsunami hazards in the California Continental Borderland (1795A). *Professional Paper*, i–31. https://doi.org/10.3133/pp1795A

Saikia, U., Rychert, C., Harmon, N., & Kendall, J. M. (2020). Sediment structure at the equatorial mid-atlantic ridge constrained by seafloor admittance using data from the PI-LAB experiment. *Marine Geophysical Researches*, *41*(1), 3. https://doi.org/10.1007/s11001-020-09402-0

Sella, G. F., Dixon, T. H., & Mao, A. (2002). Revel: A model for recent plate velocities from space geodesy. *Journal of Geophysical Research*, *107*(B4), 30. https://doi.org/10.1029/2000JB000033

Seton, M., Müller, R. D., Zahirovic, S., Gaina, C., Torsvik, T., Shephard, G., et al. (2012). Global continental and ocean basin reconstructions since 200Ma. *Earth-Science Reviews*, *113*(3), 212–270. https://doi.org/10.1016/j.earscirev.2012.03.002

Shen, W., Ritzwoller, M. H., Schulte-Pelkum, V., & Lin, F.-C. (2013). Joint inversion of surface wave dispersion and receiver functions: A Bayesian Monte-Carlo approach. *Geophysical Journal International*, *192*(2), 807–836. https://doi.org/10.1093/gji/ggs050

Shillington, D. J., Bécel, A., Nedimović, M. R., Kuehn, H., Webb, S. C., Abers, G. A., et al. (2015). Link between plate fabric, hydration and subduction zone seismicity in Alaska. *Nature Geoscience*, *8*(12), 961–964. https://doi.org/10.1038/ngeo2586

Stabeno, P. J., Bond, N. A., Hermann, A. J., Kachel, N. B., Mordy, C. W., & Overland, J. E. (2004). Meteorology and oceanography of the northern Gulf of Alaska. *Continental Shelf Research*, *24*(7), 859–897. https://doi.org/10.1016/j.csr.2004.02.007

Stevenson, A. J., Scholl, D. W., & Vallier, T. L. (1983). Tectonic and geologic implications of the Zodiac fan, Aleutian abyssal plain, northeast Pacific. *GSA Bulletin*, *94*(2), 259–273. https://doi.org/10.1130/0016-7606(1983)94<259:TAGIOT>2.0.CO;2

Straume, E. O., Gaina, C., Medvedev, S., Hochmuth, K., Gohl, K., Whittaker, J. M., et al. (2019). GlobSed: Updated total sediment thickness in the world's oceans. *Geochemistry, Geophysics, Geosystems*, *20*(4), 1756–1772. https://doi.org/10.1029/2018GC008115

Takagi, R., & Nishida, K. (2022). Multimode dispersion measurement of surface waves extracted by multicomponent ambient noise cross-correlation functions. *Geophysical Journal International*, *231*(2), 1196–1220. https://doi.org/10.1093/gji/ggac225

Tape, C. (2022). Documentation and digital files in support of "Aftershock regions of Aleutian–Alaska megathrust earthquakes, 1938–2021" by Carl Tape and Anthony Lomax: Parts B, C, and D (Version 1.0) [Dataset]. *Zenodo*. https://doi.org/10.5281/ZENODO.6274314

Tian, Y., Shen, W., & Ritzwoller, M. H. (2013). Crustal and uppermost mantle shear velocity structure adjacent to the Juan de Fuca Ridge from ambient seismic noise. *Geochemistry, Geophysics, Geosystems*, *14*(8), 3221–3233. https://doi.org/10.1002/ggge.20206

Vallier, T. L., Scholl, D. W., Fisher, M. A., Bruns, T. R., Wilson, F. H., Huene, R., & Stevenson, A. J. (1994). Geologic framework of the Aleutian arc, Alaska. In G. Plafker & H. C. Berg (Eds.), *The geology of Alaska*, Geological Society of America. https://doi.org/10.1130/DNAG-GNA-G1.367

Vanneste, M., Sultan, N., Garziglia, S., Forsberg, C. F., & Heureux, L. (2014). Seafloor instabilities and sediment deformation processes: The need for integrated, multi-disciplinary investigations. *Marine Geology*, *352*, 183–214. https://doi.org/10.1016/j.margeo.2014.01.005

Wang, F., Wei, S. S., Connor, E., Julie, L., Freymueller, J. T., Ruppert, N. A., & Zhang, H. (2024). Fluids control along-strike variations in the Alaska megathrust slip. *Earth and Planetary Science Letters*, *633*, 118655. https://doi.org/10.1016/j.epsl.2024.118655

Wang, J.-H., Chi, W. C., Nigel Edwards, R., & Willoughby, E. C. (2010). Effects of sea states on seafloor compliance studies. *Marine Geophysical Researches*, *31*(1), 99–107. https://doi.org/10.1007/s11001-010-9091-z

Wang, Y., Li, Z., You, Q., Hao, T., Xing, J., Liu, L., et al. (2016). Shear-wave velocity structure of the shallow sediments in the Bohai Sea from an ocean-bottom-seismometer survey. *Geophysics*, *81*(3), ID25–ID36. https://doi.org/10.1190/geo2015-0417.1

Webb, S. C., & Barclay, A. H. (2023). Optimizing Ocean bottom seismometers for shallow water using shielding and horizontal pressure gradient data. *Journal of Geophysical Research: Solid Earth*, *128*(8), e2023JB026356. https://doi.org/10.1029/2023JB026356

Wei, S. S., Philipp, G., Sydney, L., Huggins, E. G., Ruppert, N., Gao, L., & Zhang, H. (2021). Along-strike variations in intermediate-depth seismicity and arc magmatism along the Alaska Peninsula. *Earth and Planetary Science Letters*, *563*, 116878. https://doi.org/10.1016/j.epsl.2021.116878

Welch, P. (1967). The use of fast Fourier transform for the estimation of power spectra: A method based on time averaging over short, modified periodograms. *IEEE Transactions on Audio and Electroacoustics*, *15*(2), 70–73. https://doi.org/10.1109/TAU.1967.1161901

Williams, E. F., Fernández-Ruiz, M. R., Magalhaes, R., Vanthillo, R., Zhan, Z., González-Herráez, M., & Martins, H. F. (2021). Scholte wave inversion and passive source imaging with ocean-bottom DAS. *The Leading Edge*, *40*(8), 576–583. https://doi.org/10.1190/tle40080576.1

Zha, Y., & Webb, S. C. (2016). Crustal shear velocity structure in the Southern Lau Basin constrained by seafloor compliance. *Journal of Geophysical Research: Solid Earth*, *121*(5), 3220–3237. https://doi.org/10.1002/2015JB012688

Zhang, Z., & Olugboji, T. (2021). The signature and elimination of sediment reverberations on submarine receiver functions. *Journal of Geophysical Research: Solid Earth*, *126*(5), e2020JB021567. https://doi.org/10.1029/2020JB021567

Zheng, M. (2024). MCMC_Compliance: Markov Chain Monte Carlo inversion of seafloor compliance (version 0.0.1) [Software]. *Zenodo*. https://doi.org/10.5281/zenodo.13921936

Zheng, M., Sheehan, A., Liu, C., Wu, M., & Ritzwoller, M. (2024). Seismic model of the seafloor sediment and shallow oceanic crust of the Alaska-Aleutian subduction zone at the Alaska peninsula [Dataset]. *Zenodo*. https://doi.org/10.5281/zenodo.13921995

Zhu, J., Canales, J. P., Han, S., Carbotte, S. M., Arnulf, A., & Nedimović, M. R. (2020). Vp/Vs ratio of incoming sediments off Cascadia subduction zone from analysis of controlled-source multicomponent OBS records. *Journal of Geophysical Research: Solid Earth*, *125*(6), e2019JB019239. https://doi.org/10.1029/2019JB019239

Zimmermann, M., Prescott, M. M., & Haeussler, P. J. (2019). Bathymetry and Geomorphology of Shelikof strait and the western Gulf of Alaska. *Geosciences*, *9*(10), 409. https://doi.org/10.3390/geosciences9100409